Comparison of Microstructures and Properties for a Ni-Base Superalloy (Alloy 625) Fabricated by Electron and Laser Beam Melting

K. N. Amato, J. Hernandez, L. E. Murr, E. Martinez, S. M. Gaytan & P. W. Shindo

Department of Metallurgical and Materials Engineering

The University of Texas at El Paso, El Paso, TX 79968, USA

E-mail: knamato@miners.utep.edu

S. Collins

Directed Manufacturing, North Austin, TX 78660, USA

Abstract

Nickel-based superalloys processed by additive manufacturing have demonstrated directional solidification, which has been shown to equal or improve mechanical properties compared to cast and wrought alloys. Inconel 625 cylinders have been manufactured by electron beam melting (EBM) and selective laser melting (SLM) and compared. EBM cylinders were built in the Z-axis direction (parallel to the build direction), and SLM cylinders were built in XY-axis (perpendicular to build direction) and Z-axis directions. The microstructures of as-fabricated as well as fabricated and HIPed cylinders were characterized by light optical metallography (LOM), X-ray diffraction (XRD), scanning electron microscopy (SEM), transmission electron microscopy (TEM), and energy-dispersive (X-ray) spectroscopy (EDS). EBM fabricated components contained columnar plates of γ'' (Ni_3Nb) precipitates while SLM components contained columnar arrays of fine γ'' nanoparticles. The EBM fabricated and HIPed samples and SLM fabricated and HIPed samples exhibited equiaxed grains, but both components contained complex arrays of dissimilar precipitates.

1. Introduction

Over the past decade a variety of additive-layer manufacturing technologies employing electron and laser beam fabrication have demonstrated novel prospects for developing complex and multifunctional components with applications in biomedical, aeronautical, and automotive areas (Cormier, *et al.*, 2004; Murr, *et al.*, 2009; Murr, *et al.*, 2012a). In contrast to more conventional metal or alloy fabrication involving cast or wrought processing, electron and laser beam processing, especially electron beam melting (EBM) and selective laser melting (SLM) involve new directional solidification concepts as well as novel prospects for microstructure control through the development of scanning strategies or related process variables (Thijs, *et al.*, 2010; Bontha, *et al.*, 2009). These features produce solidification cooling rate and thermal gradient phenomena which contribute to microstructure and microstructural architecture development and resulting mechanical properties.

Thijs *et al.* (2010) have shown that laser beam scan speed and beam power can control grain orientation and martensitic transformation in Ti-6Al-4V alloy. Similar phenomena have been demonstrated in the development of solidification maps to investigate trends in grain size and morphology in Ti-6Al-4V by Bontha *et al.* (2009). Murr *et al.* (2009) have compared Ti-6Al-4V microstructures for EBM and SLM fabrication where the more rapid SLM solidification cooling produced a propensity of α'-martensite. More recent observations of EBM and SLM fabrication of Ni-base and Co-base superalloys have demonstrated the development of columnar precipitates formed within the micron-size melt pools along with textured, columnar grains in the fcc matrix (Gaytan, *et al.*, 2010; Murr, *et al.*, 2011). Similar texturing of martensite laths has also recently been observed in the SLM fabrication of 17-4 PH stainless steel as well (Murr, *et al.*, 2012b). In these studies, EBM fabrication

involved connected melt pools measuring 2-3 μm while SLM fabrication involved melt pool dimensions ~1 μm. EBM scanning differs from SLM scanning in fundamental ways which include the energy absorption and deposition within the additively-formed powder bed layers, beam focus and scan spacing, as well as powder bed pre-heat scanning and multiple or re-melt scanning. These thermo-kinetic phenomena can influence precipitate or other phase development and transformation in complex ways which differ notably from more conventional thermo-processing.

Strondel *et al.* (2008) observed γ''-Ni$_3$Nb (bct) precipitate columns in alloy 718 fabricated by EBM while Amato *et al.* (2012) observed similar precipitate columns formed in alloy 718 fabricated by SLM. Textured [200] γ-fcc matrix grains elongated in the build direction were also observed in these studies of alloy 718 while the γ'' precipitate discs were coincident with the γ-fcc matrix {100} planes. Similarly, Murr *et al.* (2011) observed γ''-bct Ni$_3$Nb precipitate platelets coincident with γ-fcc matrix {111} planes arranged in columnar arrays parallel to the build direction for alloy 625 fabricated by EBM. This difference in matrix plane coincidence portends a fundamental difference in directional solidification for EBM versus SLM fabrication. Hot isostatic pressing (HIPing) of these EBM-fabricated alloy 625 components dissolved the γ'' precipitates, forming non-coherent laves (hexagonal) NbCr$_2$ globular, polyhedral precipitates along with non-coherent, bcc Cr inclusions. Both of these phases were distributed within the grain boundaries and the matrix of the HIPed components.

In the present study we compared the precipitation and columnar grain development in alloy 625 fabricated by EBM and SLM, along with associated microstructures and corresponding mechanical behavior: tensile and hardness properties. Microstructures, particularly precipitation features developed during HIPing of the EBM and SLM-fabricated alloy 625 were also examined along with the resulting mechanical properties. Light optical microscopy (LOM), scanning and transmission electron microscopy (SEM and TEM) and X-ray diffraction (XRD) were used to characterize the associated and comparative microstructures and microstructural architectures represented by columnar precipitate arrays.

2. Process Comparison and Experimental Methods

2.1 EBM and SLM Processing

Schematic views of the electron beam melting (EBM) and selective laser melting (SLM) systems are shown in Figure 1(a) and 1(b), respectively. Since 2005, these systems have been commercially available. Cylinders fabricated for the research presented herein were manufactured using an Arcam A2 EBM system from Arcam AB (Sweden) and an EOS M270 SLM system from EOS GmbH (Germany). Both systems feed powder onto a bed from cassettes in a compacted layer via raking or rolling. These layers, several particles thick, are scanned and selectively melted by an electron or laser beam (as shown in Figure 1(a) and (b), respectively). Figure 1(c) shows the microdendritic structure and variance in particle size of the Inconel 625 powder that is rapidly solidified in an inert environment such as argon or nitrogen. The distribution of particle sizes and near-spherical shape (Figure 1(c)) increases the efficiency in flow and layer packing as well as a more uniform melt. Table 1 compares the elemental analyses for the EBM and SLM powders and representative fabricated components. The average powder sizes were measured to be 22μm and 20μm for the EBM and SLM powder, respectively.

In the EBM system (Figure 1(a)), an electron beam is generated in an electron gun (1) where it is focused through an elecromagnetic lens system (2) after being accelerated by a 60 kV potential. The beam, directed by an embedded CAD program (3), selectively melts the powder. The powder bed is preheated to $0.8T_m$ (T_m is the melting temperature) with a high beam current (~30mA) and multiple passes of the beam at a scan rate of ~10^4 mm/s. The scan rate is reduced to ~10^2 mm/s and the current is reduced to ~5 to 10 mA for the final melt scan, which produces melt pools with a size determined by the beam diameter and scan spacing. After the build table (7) has been preheated, powder is gravity fed onto it from cassettes (4) and raked (5) in an even layer. The build table moves downward after each successive layer of the component (6) has been melted. The build direction is indicated by the arrow B in Figure 1(a), which is in the z-direction in relation to the x-y scan direction of the powder layers. The EBM system operates in under a vacuum of <10^{-4} Torr. To enhance heat conduction and component cooling, the pressure is increased to ~10^{-2}Torr by a helium gas bleed near the build area.

In the SLM system (Figure 1(b)), a 100 μm diameter laser beam (1), which is scanned by a rotating mirror system (2) and driven by an embedded CAD program is focused onto a powder bed (3). The EOS M270 system operates with a 0.2 kW Yb: YAG fiber laser. The powder layer is formed by a mechanical recoater (4) onto the build platform (5) when the powder is fed from a supply container (6). Excess powder is recycled from (7). The build platform is heated to ~90°C and is maintained at this temperature during building, unlike the EBM process. The beam scan rate during melting is between 800 and 1200 mm/s and scans in the x-y direction or can alternate in the x or y directions for each layer. Rather than operating under vacuum, the SLM system is controlled in a

purified N_2 environment to provide oxidation resistance by purging oxygen from the system while providing efficient heat conduction and component cooling. Similar to the EBM system, the beam scan speed, beam width, scan spacing, and scan strategies (directional or orthogonal x-y scans) may be adjusted to alter the microstructure of the alloy. Furthermore, the melt scan can remelt the layer if rescanned and the beam can re-heat the layer in a process anneal if adjusted.

2.2 Structural and Microstructural Analyses

Microstructures of Inconel 625 powders and cylinders fabricated by EBM and SLM were examined using LOM and XRD before SEM and TEM analyses. Elemental analyses and mapping was conducted from EDS attachments on the SEM and TEM. TEM analyses included selected area diffraction (SAED) and dark-field imaging. As-fabricated cylinders HIPed at 1120°C at 0.1 GPa pressure for 4 h in argon were also analyzed using the same processes.

Transverse (horizontal) and longitudinal (vertical) coupons were cut from the EBM- and SLM-processed cylinders which were then mounted in an epoxy-base material. Inconel 625 powder (Figure 1 (c)) was mounted as well. After being ground and polished, samples were electro-etched in a solution of 70 mL phosphoric acid and 30 mL water, at room temperature, using 5 V for times ranging from 5s to 2 min. To bring out annealing twin structures, samples were additionally electro-etched with 5% hydrochloric acid for 1-10s. A Reichert MEF4 A/M metallograph was used to conduct LOM on etched samples.

XRD spectra of the precursor powder (Figure 1 (c)) as well as coupons from horizontal and vertical planes of as-fabricated and fabricated and HIPed cylinders were obtained using a Bruker AXS-D8 Discover system with a Cu target.

SEM images were taken in both secondary and backscatter electron image modes from a Hitachi S-4800 field emission (FE) SEM operated at 20 kV. EDS was performed on an EDAX-EDS system fitted onto the SEM. For TEM analysis, coupons extracted as previously mentioned were ground and polished to a thickness of ~200 μm and punched into 3mm discs. The discs were electropolished in a Tenupol-5 dual jet system at temperatures ranging from -26 to -28°C at 13 V in an electropolishing solution containing 200mL perchloric acid and 800mL methanol. TEM analysis was achieved with a Hitachi H-9500 high-resolution TEM operated at 300 kV, which included a fitted goniometer-tilt stage, a digital imaging camera, and an EDAX-EDS elemental (X-ray) mapping analysis attachment (EDAX r-TEM[TM] detector).

2.3 Mechanical Testing

Microhardness and macrohardness measurements were made on coupons extracted from horizontal and vertical planes of as-fabricated and HIPed specimens as well as the mounted, polished, and etched precursor powder. The microindentation (Vickers) hardness (HV) was measured with a Vickers diamond indenter in a Shimadzu HMV=2000 tester (using 25 and 100 gf or 0.25 N and 1 N load, respectively, for ~10s load time). Macrohardness measurements were taken from a Rockwell tester with a 1.5 N load and a C-scale indenter (HRC).

Tensile specimens were machined from the as-fabricated and as-fabricated and HIPed EBM cylinders as well as the SLM HIPed cylinders. Tensile specimens were machined from the as-fabricated cylinders HIPed at 0.1 GPa for 4 h at 1120°C (~$0.84T_m$, where T_m was 1335°C). Tensile tests were conducted in an upgraded Tinius-Olsen Universal Testing machine (SIN 175118) at a strain rate of ~$10^{-3}\,s^{-1}$ at room temperature (22°C). The fabricated and HIPed specimens were also tested at 538°C (1000°F). Fracture surfaces were also examined in the SEM.

3. Results and Discussion

3.1 Microstructural Characterization of EBM-Fabricated Components

Figure 2 shows a 3D LOM composition typical for columnar Ni_3Nb (bct: a = 0.362 nm, c = 0.741 nm; space group: I4/mmm) γ″-precipitate platelets oriented in the build direction (arrow in Figure 2), and corresponding to roughly 2 μm melt pool dimensions characteristic of the EBM beam scan geometry. Figure 3 shows a TEM magnified view of the Ni_3Nb (γ″) precipitate platelets which are coincident with the NiCrγ-matrix (fcc, a = 0.359 nm; space group: Fm$\bar{3}$m) {111} planes as discussed in detail by Murr *et al.* (2011). Note in Figure 3 that the γ″ platelets are associated with columnar, low-angle boundaries which help to define the columnar arrays. Dense dislocation substructures are also observed to be associated with the precipitates. The columnar precipitate arrays shown in Figures 2 and 3 are also oriented (textured) in the [200] direction parallel to the build direction. These columnar arrays are also coincident with the as-fabricated cylinder (Z) axis as evident from the XRD spectrum shown for the horizontal section perpendicular to the build direction (B in Figures 2 and 3) in Figure 4. The vertical section XRD spectra also show the [220] texture in the plane parallel to the build direction in Figure 2,

and is coincident with the [110] zone corresponding to Figure 3. The Ni$_3$Nb (bct) precipitate platelet spectra coincide with fcc (γ)-NiCr peaks noted in Figure 4.

Columnar grains, primarily oriented in the [200] direction shown in the XRD spectra in Figure 4, are roughly 10 μm in diameter as shown lightly etched in the 3D LOM composition in Figure 2.

3.2 Microstructures for EBM-Fabricated and HIP Components

Figure 5 shows a 3D LOM image composition for the EBM-fabricated and HIP components showing characteristic equiaxed grains and annealing twins representing the low-stacking-fault free energy fcc-NiCr matrix (Murr, 1975). The average grain size was observed to be ~50 μm, including the annealing twins. The matrix contains a dense distribution of precipitates along with continuous precipitate arrays in many grain boundaries presumed to be high energy (Murr, 1975). Figure 6 shows the corresponding XRD spectra for Figure 5, where dark (shaded) peaks represent the precipitation: NbCr$_2$ (laves: hexagonal; a = 0.49 nm, c = 0.81 nm, space group: P63 mmc), nickel-rich, Ni$_8$Nb (tetragonal; a = 0.76 nm, c = 0.36 nm; space group: P(0)); and pure Cr precipitates. These are represented typically in the TEM image in Figure 7, which shows a low-energy annealing twin with no precipitation in the boundaries (Murr, *et al.*, 2011). In contrast, Figure 8 shows an analytical sequence showing a Cr inclusion (precipitate) at the edge of an electropolished foil section. The bright-field TEM image in Figure 8(a) is in a (110) grain orientation shown by the SAED pattern in Figure 8(b). Figure 8(c) shows the precipitate EDS analysis in contrast to the matrix EDS analysis shown in Figure 8 (f); in contrast to Table 1. Figure 8(d) and (e) show corresponding Cr and Ni elemental maps utilizing the EDS analysis in Figure 8(c).

3.3 Mechanical Behavior for EBM-Fabricated and HIP Components

Components built by EBM included only cylinders fabricated in the Z-axis direction (cylinder axis) and parallel to the build direction. Tensile specimens for the as-fabricated (Z-axis) specimens as well as as-fabricated and HIP specimens exhibited typical properties shown for comparison in Table 2. Table 2 also compares Vickers microindentation hardness (HV) measurements and Rockwell C-scale (HRC) macroindentation measurements for these fabricated and processed specimens. There is a corresponding hardness drop following HIP, along with a drop in yield stress (YS) but the ultimate tensile stress is not significantly affected. There is a significant increase in elongation after HIP: 69% versus 44% as-fabricated; an increase of ~57%. This considerable elongation is characterized by classical ductile-dimple fracture as illustrated typically in Figure 9(b). Typical elongation of Z-axis oriented tensile specimens for as-fabricated and HIP specimens is shown in Figure 9(a).

Examination of the deformation associated with, and as a precursor to fracture, showed dense, generally linear dislocation arrays in {111} planes of the fcc-NiCr matrix as illustrated in Figure 10. The dislocation density in Figure 10 can be compared with that typical for as-fabricated EBM components shown in Figure 3, where the dislocation density difference is more than an order of magnitude.

3.4 Microstructural Characterization of SLM-Fabricated Components

Figure 11 shows a 3D LOM image composition typical for the as-fabricated, Z-axis oriented cylinders built in the direction parallel to the cylinder axis. In contrast to Figure 2 at the same magnification, there are several very notable differences. First is the presence of melt (layer) banding characteristic of laser melt scanning (Thijs *et al.*, 2010). The dark contrast which distinguishes these bands arises by enhanced precipitation of γ″ (bct-Ni$_3$Nb). Second, and in the context of γ″ precipitation, it is readily apparent in Figure 11 that the columnar precipitate arrays are roughly half or less the γ″ precipitate column spacing for EBM components shown in Figure 2. The actual γ″ column array widths are also roughly 3 times those for SLM-fabricated (Z-axis) components as shown in Figure 11.

The precipitates in the columnar arrays of Figure 11 are also not large platelets or discs similar to those shown in Figures 2 and 3. Additionally, and as shown in Figure 12 in contrast to the XRD spectra in *Figure* 4, the orientation in the horizontal reference plane normal to the build direction is [200], while for the vertical reference plane parallel to the build direction, the orientation is also [200] for SLM (Figure 12) and [220] for EBM fabrication (Figure 4). Note that, as in the XRD spectra for EBM-fabricated (Z-axis) components in Figure 4, the γ″ (bct-Ni$_3$Nb) precipitate phase spectra coincide with select fcc-NiCr spectral peaks.

In contrast to Z-axis built components, cylindrical components were also built in the X-Y plane perpendicular to the build direction. These X-Y (or XY)-axis components exhibited similar macrostructure-microstructure features to those shown in Figure 11 for Z-axis built, SLM components. Figure 13 shows a slightly more magnified 3D LOM image composition than Figure 11 showing irregular, columnar precipitate arrays along with oriented, low-angle grain boundaries (6B) and characteristic SLM melt-scan banding. Again, it is especially

notable to recognize the difference between the γ″ precipitate columns for EBM in Figure 2 and the γ″ precipitate columns for SLM in Figure 13. The XRD spectra for the horizontal and vertical reference planes in Figure 13 (indicated by H and V, respectively) are also shown in Figure 14 which, as noted previously for Figure 12, shows different, preferred orientations or textures than those exhibited for EBM-fabricated components shown in Figure 4. The prominence of [111] and [200] are particularly notable for SLM component texture (Figure 14).

Figure 15(a) and (b) illustrate the significant difference in γ″ precipitate morphology and size for the SLM fabricated cylinders (XY-axis) in contrast to those shown in Figure 3 for EBM fabrication. Comparison of Figures 3 and 15(b) also illustrate the smaller precipitate column spacing for SLM versus EBM-fabricated components. Similar, dense dislocation arrays are also associated with the very fine (nano-size) γ″ precipitate columnar arrays as shown in Figure 15(b). Examination of Figure 15(a) and (b) in contrast to Figure 13 suggests that the precipitate columns form as cylindrical arrays at the edges or transition regions of the melt pools, rather than the center of the melt pools. The (112) orientation for the horizontal reference plane view in Figure 15(a) SAED pattern insert also demonstrates that the dislocation-precipitate arrays are dominated by the melt pool geometry rather than texture, which is dominated by [200] as shown in Figure 14.

Figure 16 shows a magnified TEM image representing the precipitate reference at P in Figure 15(b). To right in Figure 16 the fine γ″ precipitates and heavy dislocation substructure composing the columnar arrays prominently depicted in Figure 13. The precipitates at P in Figure 16 appear to be a small cluster of three γ″ precipitate particles with diameters ranging from 10 to 20 nm. Somewhat larger precipitates are shown in the column to the right in Figure 16, and there is evidence for precipitation on dislocations as well.

Figures 17 and 18 show a sequence of analytical components which examine the composition of the fine γ″ precipitates In Figure 17, a vertical reference section of an XY-oriented cylinder is examined in the TEM. The small section of a precipitate column shown bounded by the dashed-line box is magnified in Figure 18(a). While arrows delineate a short section of precipitates in Figure 18(a) and (b), where Figure 18(b) represents a Nb X-ray map using the Nb window for the EDS (elemental) spectra shown in Figure 18(c). Because of the very small size of the globular, nano-precipitates (γ″), there is no discernable Ni signal associated with the 100 nm long strip between the arrows in Figure 18(a) and (b).

It might also be noted that the selected-area electron diffraction (SAED) pattern for the TEM image area shown in Figure 3 for γ″ precipitate columns in an EBM fabricated component was indexed with a [220] (or [110]) zone axis, and the corresponding crystallographic directions are noted in Figure 3. Correspondingly, the SAED pattern inserts in both Figures 15 and 17 for corresponding TEM images in an SLM-fabricated component are also a [110] zone axis. Again, comparing these common crystallographic features in Figures 3 and 15 point up the notable difference in γ″ precipitate morphology and size discussed above for EBM versus SLM fabrication. This is due in large part because of the notable difference between the cooling or solidification phenomena, where SLM beam scan produces considerably more rapid cooling (Murr, *et al.*, 2009; 2012a) which appears to restrict precipitate nucleation and growth. This is also exaggerated by building X-Y-oriented cylinders which cool much differently from the Z-axis oriented cylinders. Beam scan and especially melt scan variances are especially notable on comparing Figures 2 and 11. Figure 19 compares LOM and SEM images showing the vertical reference plane melt-scan-related banding for SLM-fabricated components. The γ″ precipitates which delineate these bands are illustrated more prominently in the SEM image of Figure 19(b).

3.5 Microstructures for SLM-Fabricated and HIP Components

Figures 20 and 21 show 3D LOM image composites for SLM cylindrical components fabricated in the Z-axis direction and XY-axis directions and HIPed, respectively. Although the HIP-annealed microstructures shown in Figs. 20 and 21 emulate the equiaxed NiCr grain structure containing coherent annealing twins or twin boundaries shown for EBM fabricated-HIP samples shown represented typically in Figure 5, there are notable differences. The most notable difference is the apparently larger intergranular precipitates, with the largest precipitates shown in Figure 20. Precipitation in the grain boundaries occurs in a similar fashion with continuous precipitation or second-phase appearance along some boundaries. There is no precipitation along the low-energy, coherent twin boundaries in either Figures 5, 20, or 21.

As shown in the XRD spectra for corresponding horizontal and vertical reference planes for EBM-fabricated and HIP components in Figure 6, and in supporting data contained in Figures 7 and 8 precipitation involves $NbCr_2$ (hexagonal; space group: P_{63}/mmc; a = 4.98 Å, c = 8.06 Å) laves precipitates, pure (bcc) Cr precipitates, and Ni_8Nb (tetragonal) precipitates (Murr, *et al.*, 2011). In contrast, the XRD spectra corresponding to Figs. 20 and 21 shown in Figure 22 and 23, respectively, indicate smaller amounts of $NbCr_2$ (hexagonal) laves precipitates,

MoNb (bcc) precipitates and NiNb (rhombohedral) precipitates. These findings are consistent with the fundamental differences in microstructures developed in EBM versus SLM-fabricated components. The large, intergranular precipitates shown in Figure 20 are MoNb polyhedra having sizes ranging from 0.2 μm to ~1 μm. Figures 24 and 25 illustrate analysis sequences using SEM and EDS in the SEM for SLM– Z-axis fabricated and HIP components. Figures 24(e) and 25(a) clearly show the faceted, polyhedral MoNb single-crystal precipitates remaining after LOM etch. In contrast to the background spectrum shown for comparison in Figure 8(f), the elemental spectrum in Figure 25(c) shows, the Nb and Mo peak prominence, hile the corresponding elemental X-ray maps in Figure 25(b) and (d) confirm the precipitate species shown in the XRD spectra for Figure 22. Figures 26 and 27 show a typical, similar analysis sequence for MoNb precipitates in the XY-axis fabricated and HIP components corresponding to Figure 21. In contrast to Figure 25(c), Figure 27 compares the background NiCr matrix elemental (EDS) spectrum (Figure 27(a)) in contrast to the corresponding spectrum at the precipitates in Figure 26(b), where the Mo, Nb peak prominence is apparent.

Figure 28 shows smaller, intergranular precipitates viewed in the TEM in the horizontal reference plane for an XY-oriented, fabricated and HIP component (corresponding to Figure 21). Note the faceted polyhedral which represent the nano regime for the MoNb precipitates shown in Figures 21 and 26.

Figures 29 to 31 illustrate another analytical sequence involving three precipitates indicated by P_1, P_2 and P_3, respectively in Figure 29. The inserts in Figure 29 show magnified views for precipitates P_2 and P_3, respectively, while Figure 31 shows a more detailed analysis of precipitate P_1. To some extent, all of these precipitates exhibit crystallographic faceting. All, like those precipitates in Figure 28, are noncoherent dispersoids. These precipitates represent primarily NiNb (Figure 23): rhombohedral (space group: R$\bar{3}$m), a = 4.90 Å, c = 26.64 Å.

Clusters of precipitates shown in Figure 29 range from particle sizes <10 nm to >400 nm. Those shown prominently as P_1, P_2, and P_3 in Figure 29 all exhibit crystallographic facets or polyhedral forms. The EDS analyses shown in Figure 30(a) and (b) for P_1 and P_2, respectively exhibit variations in Ni and Nb in contrast to the background (NiCr matrix) analysis shown typically in Figure 27(a), and suggesting variances in Ni-Nb stoichiometry shown for the XRD data in Figure 23. This applies to Figure 31 as well where the precipitate shown in Figures. 29 and 30 as P_1 can be associated either with Nb_5Ni (fcc; space group: Rd$\bar{3}$m; a = 11.64 Å), indexing the circled diffraction spot as [$\bar{2}\bar{4}$6], or [2$\bar{1}\bar{1}$] for NiNb in Figure 31(b). The corresponding dark-field (DF) image in Figure 31(c) using the circled reflection in Figure 31(b) corresponds to a cubic or hexahedral polyhedron viewed down a vertex. This is supported by comparing the bright-field image views in Figure 31(a) and (d), where Figure 31(d) is a tilted view of Figure 31(a).

3.6 Mechanical Behavior for SLM-Fabricated and HIP Components

Cylinders fabricated by SLM in the Z-axis direction as well as cylinders fabricated in the X, Y-axis directions and following HIP were machined into comparative tensile specimens and tested as described for the EBM specimens in section 3.3 above. As-fabricated tensile tests exhibited poor tensile properties, especially elongation as a consequence of porosity and the melt pool banding as shown in Figures 11 and 13. HIP specimens exhibited tensile behavior more comparable to the EBM components, and these measurements are shown in Table 2. Table 2 also shows the corresponding microhardness (HV) and macrohardness (HRC) measurements. It can be observed that overall the SLM fabricated and HIP components exhibited considerably higher hardness and UTS, while the elongation declined slightly. SEM fracture surface images showed similar ductile-dimple behavior as observed in Figure 9 for EBM. The elevated hardness for both the SLM-fabricated and fabricated plus HIP components (Table 2) are a consequence of the different precipitation microstructures evident in Figures 15, 24 and 26, among others; in contrast to Figures 3, 5, and 7, respectively.

3.7 Discussion and Comparison of Precipitation in EBM and SLM Processed Components

A comparison of Figures 2, 11 and 13 demonstrate that on a microscale, the development of columnar precipitation microstructures is considerably different for EBM fabrication versus SLM fabrication. At a smaller microstructural scale, this difference manifests in considerably different precipitate morphologies and sizes even though the precipitate chemistry is the same γ″, bct-Ni_3Nb. Moreover, after HIP, these processed components demonstrate even more distinguishable precipitation variances, and these are shown for comparison in Table 3. Table 2 also demonstrated that the precipitation variations shown in Table 3 might account for variations in the residual mechanical properties, particularly for HIP processed components, by precipitation hardening.

The occurrence of melt-scan banding and associated γ″ precipitation within these bands illustrated in Figures 11, 13 and 19 suggest considerably different thermo-kinetic phenomena which will influence precipitation, nucleation, growth, and stoichiometry as this relates to thermo-kinetic parameters, especially

time–at–temperature as this relates to stable and metastable phases. In this respect, the precipitate phases are all noncoherent, and apparently at equilibrium.

Although Thijs *et al.* (2010) and Bontha *et al.* (2009) have investigated the effect of process variables and size-scale on solidification microstructure-grain size and morphology as well as columnar grain orientations in Ti-6Al-4V processed by laser or electron beam fabrication, there are no comparable studies in other systems. In addition, there have been no systematic or systematic studies of precipitation phenomena in electron or laser-beam processed metal or alloy systems. Consequently, Table 3 represents the first qualitative comparison of electron and laser beam processing and related precipitation phenomena.

4. Summary and Conclusions

In both EBM and SLM processes, columnar architectures are formed parallel to the build direction by γ''bct Ni_3Nb precipitates, yet the difference in cooling rates of the melt pools in each process significantly alters the size and shape of the precipitates as well as the columnar spacing, column width, and texture. The presence of melt banding does not exist in the EBM microstructure as it does in the SLM microstructure (Figure 2 and Figure 13, respectively). The columnar architecture of the EBM as-fabricated components is composed of large γ'' platelets aligned with a texture of [220] parallel to the build direction, with columnar arrays spaced ~2 to 3 μm apart. The precipitates of the SLM as-fabricated cylinders irregular, fine Ni_3Nb precipitates with a [200] texture combined with dense dislocation arrays. The columnar precipates of SLM-fabricated component had a spacing of roughly 1μm (half or less) and one third of the column width in contrast to the EBM component.

HIPing of the EBM and SLM as-fabricated cylinders at 1120°C for 4 h recrystallized the columnar grains and formed an equiaxed fcc-NiCr grain structure containing low-energy annealing twins. The columnar γ'' arrays were dissolved during the annealing process and the formation of an $NbCr_2$ laves precipitates occurred in all fabricated and HIPed EBM cylinders. Precipitates were present in high-energy grain boundaries but absent from low-energy, coherent twin boundaries. However, intergranular MoNb precipitates (smaller in XY-oriented components) in SLM-fabricated and HIPed components were notably larger than the EBM HIPed components. These precipitates are mostly MoNb with some $NbCr_2$ and traces of Nb_5Ni and NiNb, which are not present in EBM-fabricated and HIP components. The $NbCr_2$ laves precipitates were the most prominent in the EBM-fabricated cylinder with some pure Cu precipitates and traces of Ni_8Nb.

It should be noted on comparing the mechanical behavior for Z-axis and XY-axis fabricated components by either EBM or SLM, that there is both a size factor difference for Z-axis versus XY-axis fabrication, and a corresponding cooling-rate difference, which is more notable on comparing EBM and SLM fabrication. Table 2 shows that both the Vickers microindentation hardness (HV) and Rockwell C-scale hardness (HRC) increase significantly on comparing Z-axis component fabrication by EBM versus SLM. Correspondingly, there is a significant increase on comparing SLM Z-axis fabrication with XY-axis fabrication: HV 3.4 GPa versus 4.2 GPa, respectively, or an increase of 24%. In contrast to EBM Z-axis fabrication, SLM Z-axis fabrication increases even more notably: HV 2.7 GPa to 4.2 GPa, or a 56% increase; more than twice that for the SLM Z-axis versus XY-axis fabrication. There is a corresponding increase in hardness (HV) for the HIPed components: SLM - Z-axis HIP versus EBM Z-axis-HIP; and SLM Z-axis HIP versus SLM XY-axis-HIP, although the increase was not as great (Table 2). Nonetheless, the hardness differences shown in Table 2 are indicative of both the process variances (EBM versus SLM) and the component size variances (Z-axis oriented components versus XY-axis components).

References

Amato, K. N., Gaytan, S. M., Murr, L. E., Martinez, E., Shindo, P. W., Hernandez, J., Collins, S., & Medina, F. (2012). Microstructures and mechanical behavior of Inconel 718 fabricated by selective laser melting. *Acta Mater,* in press. http://dx.doi.org/10.1016/j.actamat.2011.12.032

Bontha, S., Klingbeil, N. W., Kobryn, P. A., & Fraser, H. C. (2009). Effects of process variables and size-scale on solidification microstructure in beam-based fabrication of bulky 3D structures. *Mater. Sci. Engng. A, 513-514*, 311-318. http://dx.doi.org/10.1016/j.msea.2009.02.019

Cormier, D., Harrysson, O. L., & West, H. (2004). Characterization of H13 steel produced via electron beam melting. *Rapid Prototyping J., 10*(1), 35-41. http://dx.doi.org/10.1108/13552540410512516

Gaytan, S. M., Murr, L. E., Martinez, E. J. L., Machado, B. I., Ramirez, D. A., Medina, F., Collins, S., & Wicker, R. B. (2010). Comparison of microstructures and mechanical properties for solid and mesh cobalt-base alloy prototypes fabricated by electron beam melting. *Metall. Mater. Trans., 41A*, 3310-3327.

Murr, L. E. (1975). *Interfacial Phenomena in Metals and Alloys*. Addison-Wesley Publishing, Co, Reading, MA.

Murr, L. E., Quinones, S. A., Gaytan, S. M., Lopez, M. I., Rodela, A., Martinez, E. Y., Hernandez, D. H., Martinez, E., Medina, F., & Wicker, R. B. (2009). Microstructure and mechanical behavior of Ti-6Al-4V produced by rapid-layer manufacturing for biomedical applications. *J. Mech. Behavior Biomed. Mater.*, *2*, 20-32. http://dx.doi.org/10.1016/j.jmbbm.2008.05.004

Murr, L. E., Martinez, E., Gaytan, S. M., Ramirez, D. A., Machado, B. I., Shindo, P. W., Martinez, J. L., Medina, F., Wooten, J., Ciscel, D., Ackelid, U., & Wicker, R. B. (2011). Microstructure architecture, microstructures, and mechanical properties for a nickel-base superalloy fabricated by electron beam melting. *Metall. Mater. Trans., 42A*, 3491-3508. http://dx.doi.org/10.1007/s11661-011-0748-2

Murr, L. E., Gaytan, S. M., Ramirez, D. A., Martinez, E., Hernandez, J., Amato, K. N., Shindo, P. W., Medina, F., & Wicker, R. B. (2012a). Metal fabrication by additive manufacturing using laser and electron beam melting technologies. *J. Mater. Sci. Technol., 28*(1), in press.

Murr, L. E., Martinez, E., Hernandez, J., Collins, S., Amato, K. N., Gaytan, S. M., & Shindo, P. W. (2012b). Microstructures and properties of 17-4 PH stainless steel fabricated by selective laser melting. *Mater. Sci. Engng. A*, in press.

Strondl, A., Fischer, R., Frommeyer, G., & Schneider, A. (2008). Investigations of MX and γ'/γ'' precipitates in the nickel-based superalloy 718 produced by electron beam melting. *Mater. Sci. Engng., 480A*, 138-147.

Thijs, L., Verhaeghe, F., Craeghs, T., VanHumbeeck, J., & Kruth, J-P. (2010). A study of the microstructural evolution during selective laser melting of Ti-6Al-4V. *Acta Mater., 58*, 3303-3312. http://dx.doi.org/10.1016/j.actamat.2010.02.004

Table 1. Chemical Composition for Alloy 625 EBM and SLM Precursor Powders and Fabricated Components

Material Component	Element (wt. pct.)									
	Ni	Cr	Fe	Mo	Nb	C	Mn	Si	Al	Ti
Nominal Standard	61	22	3.2	9.0	3.5	0.02	0.1	0.1	0.2	0.3
EBM Precursor powder mass analysis	65.7	21.3	0.4	9.3	3.7	0.004	-	-	-	0.002
EBM Precursor powder EDS analysis	59.1	18.8	-	7.6	3.0	-	-	-	-	-
EBM as-fabricated Z-cylinder EDS analysis	61.1	19.2	-	8.8	4.7	-	-	-	-	-
SLM Precursor powder mass analysis	64.8	21.7	<0.1	8.9	3.5	<0.01	0.47	0.39	0.05	0.08
SLM as-fabricated X, Y cylinder EDS analysis	64.2	21.2	-	9.4	5.2	-	-	-	-	-

Table 2. Mechanical Properties for EBM and SLM Processed Alloy 625

	HV (GPa)	HRC	YS (GPa)*	UTS (GPa)†	Elongation (%)
EBM-fabricated (Z)	2.7	14	0.41	0.75	44
EBM-fabricated (Z) + HIP	2.2	8	0.33	0.77	69
SLM-fabricated (Z)	3.4	30	-	-	-
SLM-fabricated(Z)+HIP	2.9	27	0.36	0.88	58
SLM-fabricated (X,Y)	4.2	43	-	-	-
SLM-fabricated (X,Y)+HIP	3.4	21	0.38	0.90	58

* YS- 0.2% engineering offset yield stress.

†UTS- Ultimate tensile stress

Table 3. Comparative Precipitation for EBM and SLM Processed Alloy 625

EBM Fabricated	SLM Fabricated
γ'' (bct-Ni$_3$Nb) {111} coincident precipitate platelets (100 nm x 1000 nm) 2-3 μm spaced columns (irregular)	γ'' (bct-Ni$_3$Nb) globular precipitates (10 to 20 nm diameter) <1 μm spaced columns (irregular)
EBM Fabricated + HIP	SLM Fabricated + HIP
NbCr$_2$ (laves) (most prominent) Ni$_8$Nb (trace) Cr	NbCr$_2$ (laves) MoNb (most prominent) NiNb Nb$_5$Ni (trace)
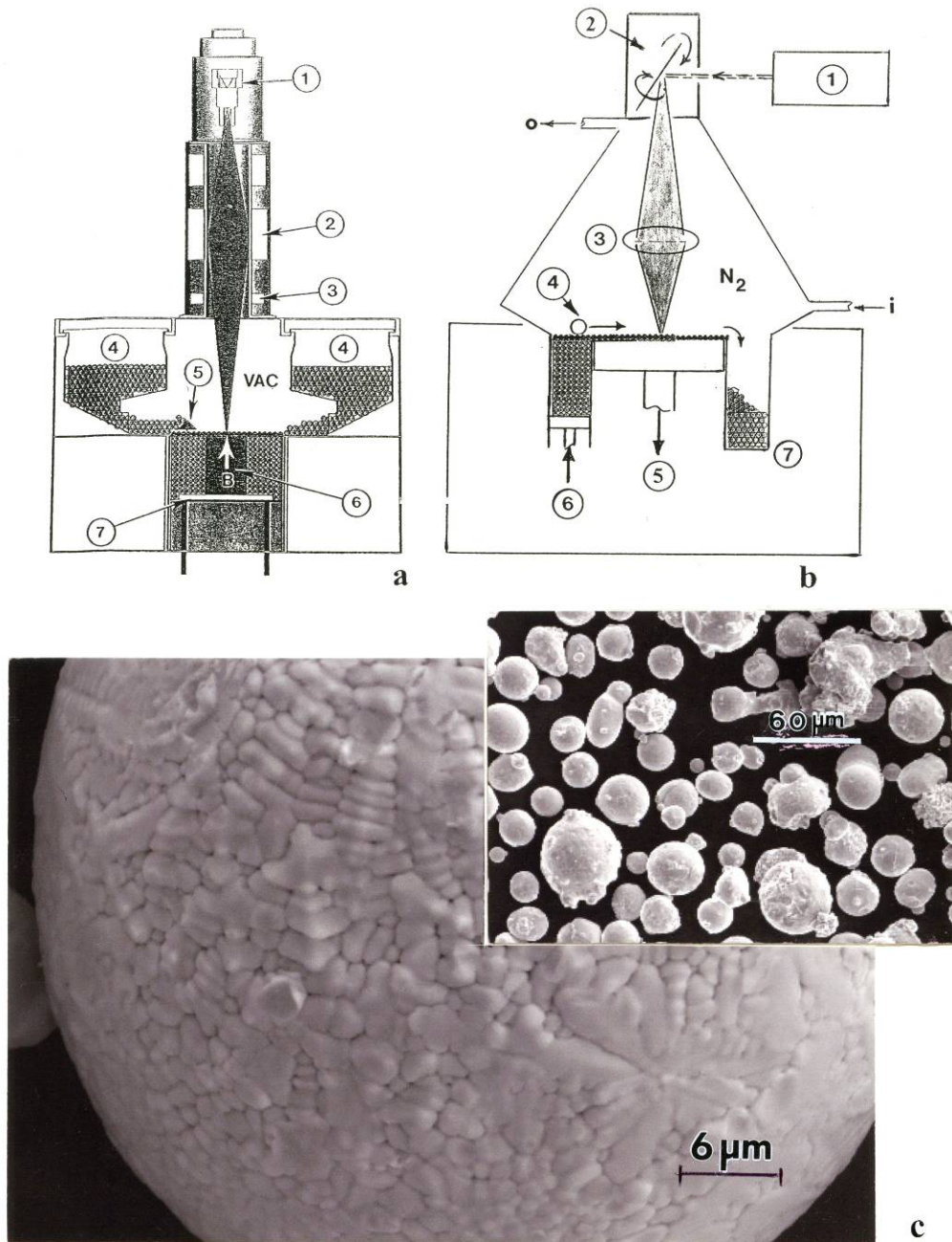
Figure 1. EBM and SLM process fundamentals. (a) EBM system schematic: Electron gun (1), Beam focus lens (2), Beam scan coils (3), Powder cassettes (4), Powder layer rake (5), Building component (6), build platform (7). (b) SLM system schematic: Laser beam source (1), Scan mirrors (2), Beam focus lens (3), Layer roller (4), Build platforms (5), Powder feed (6), Powder retrieval (7). (c), SLM powder microstructure and low magnification insert. (a) and (b) are adapted from Murr *et al.* (2012a)
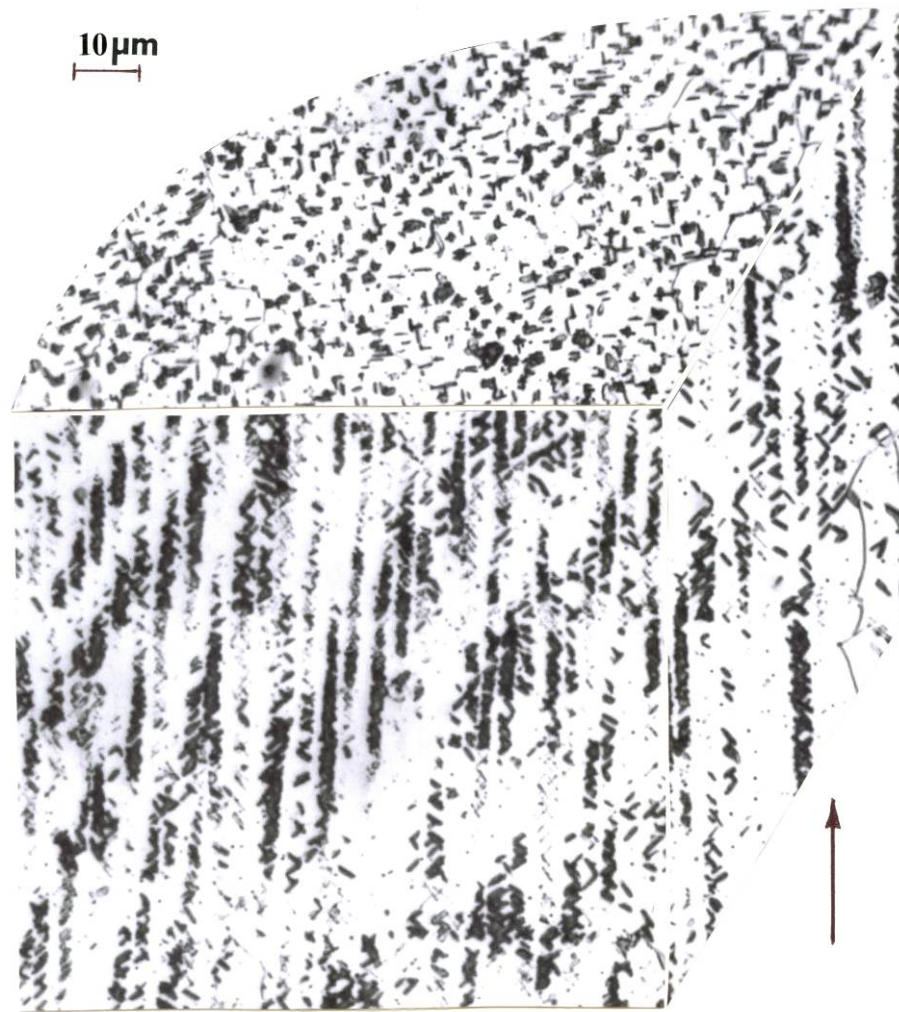
Figure 2. 3D LOM image composition for EBM fabricated component section showing columnar, precipitate platelets. Arrow at lower right shows the build direction
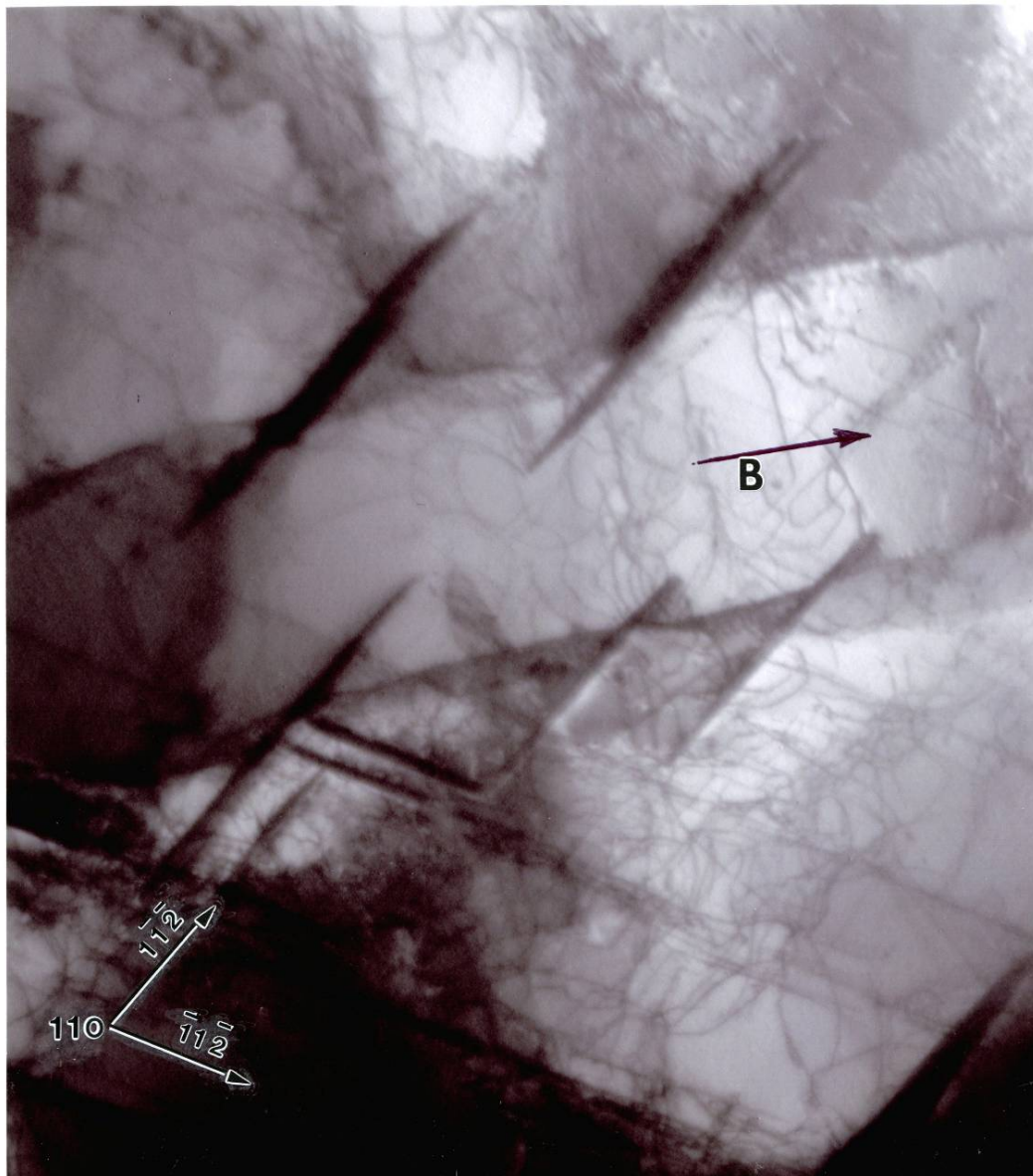
Figure 3. TEM vertical plane section view (parallel to the build direction (B) showing γ″ precipitate platelets coincident with the NiCrfcc matrix {111} planes. The grain surface orientation is (110). The build direction marked B is coincident with the arrow in Figure 2

HORIZONTAL SECTION

VERTICAL SECTION
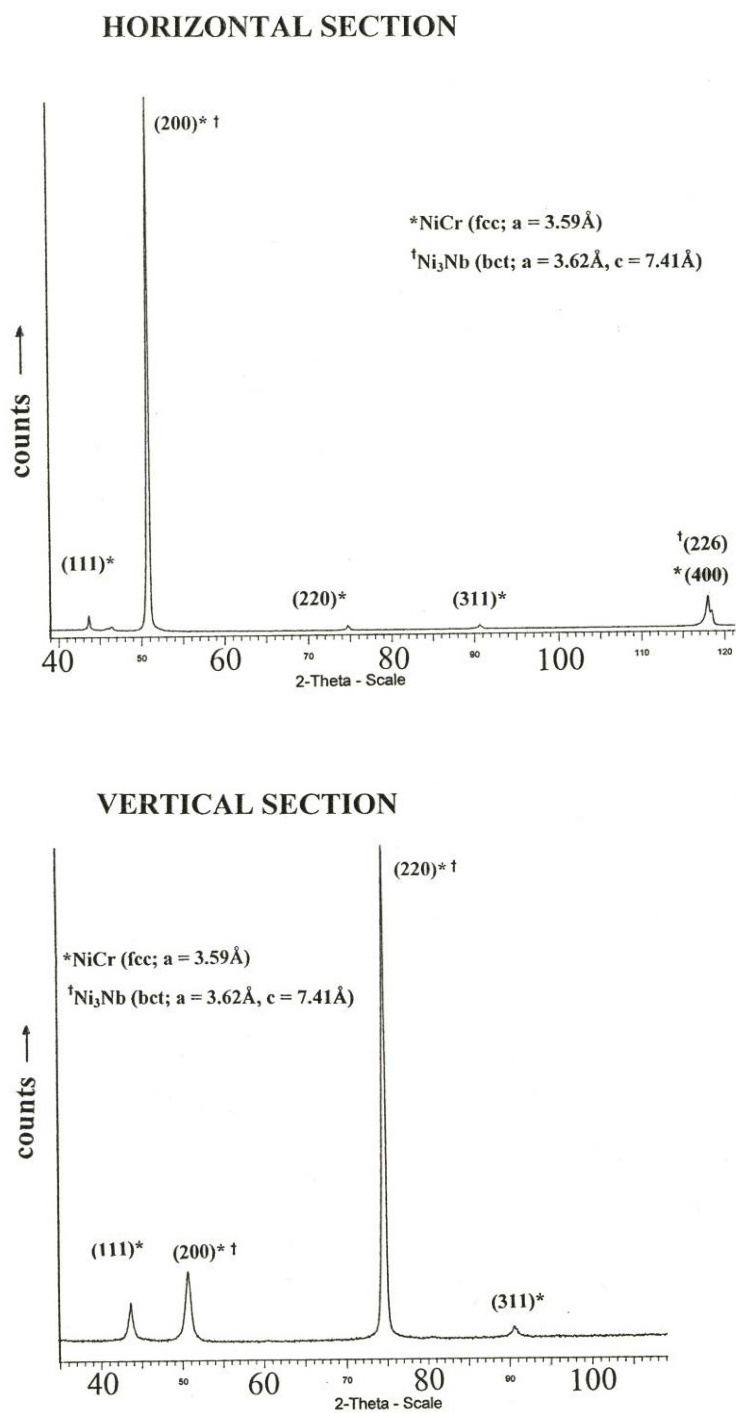
Figure 4. XRD spectra corresponding to the horizontal and vertical reference planes in Figure 2 (EBM)
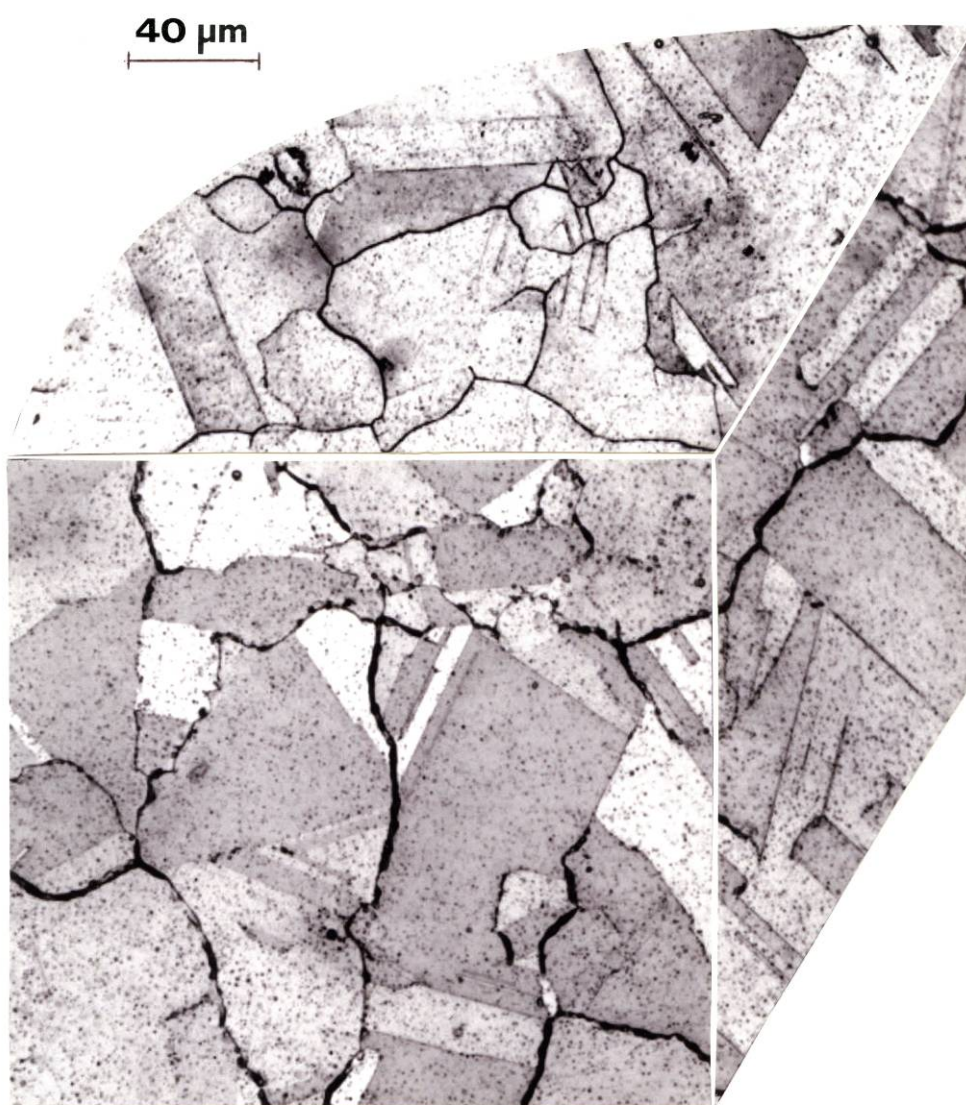
Figure 5. EBM fabricated and HIP (Z-axis) component 3D LOM composition showing equiaxed, fcc (NiCr) grain structure and associated precipitation
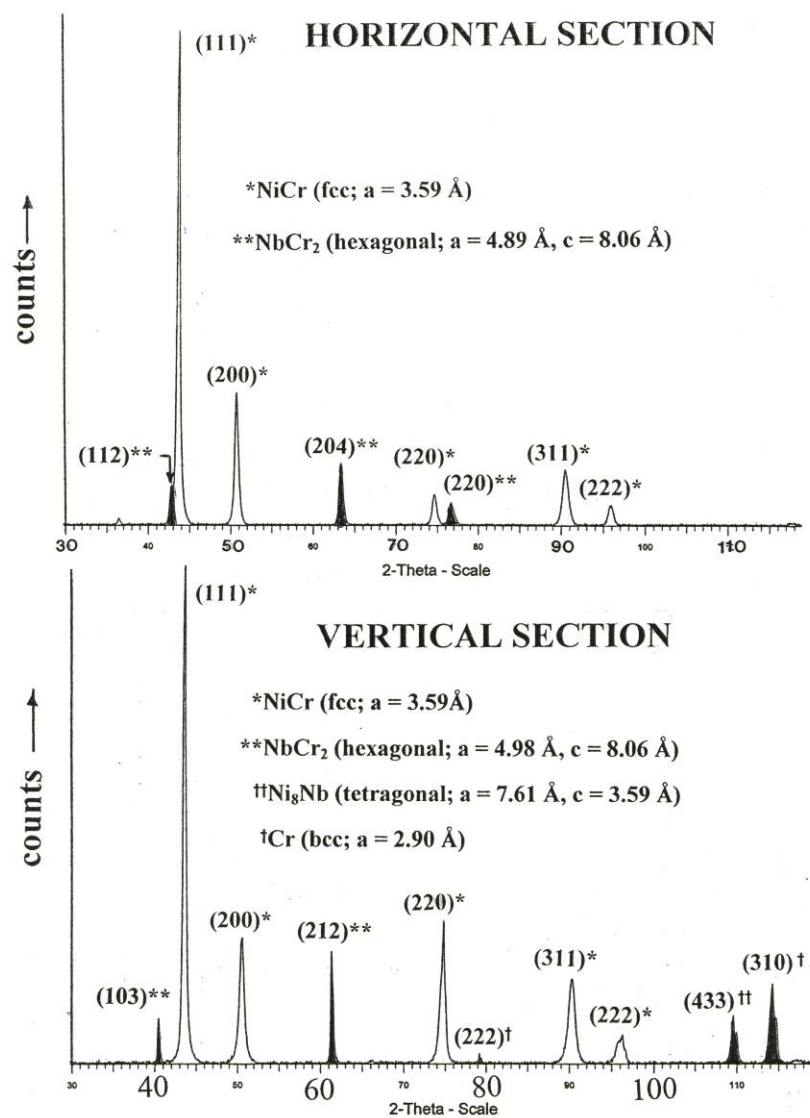
Figure 6. XRD spectra corresponding to the horizontal and vertical reference planes in Figure 5. Prominent precipitation peaks are dark shaded
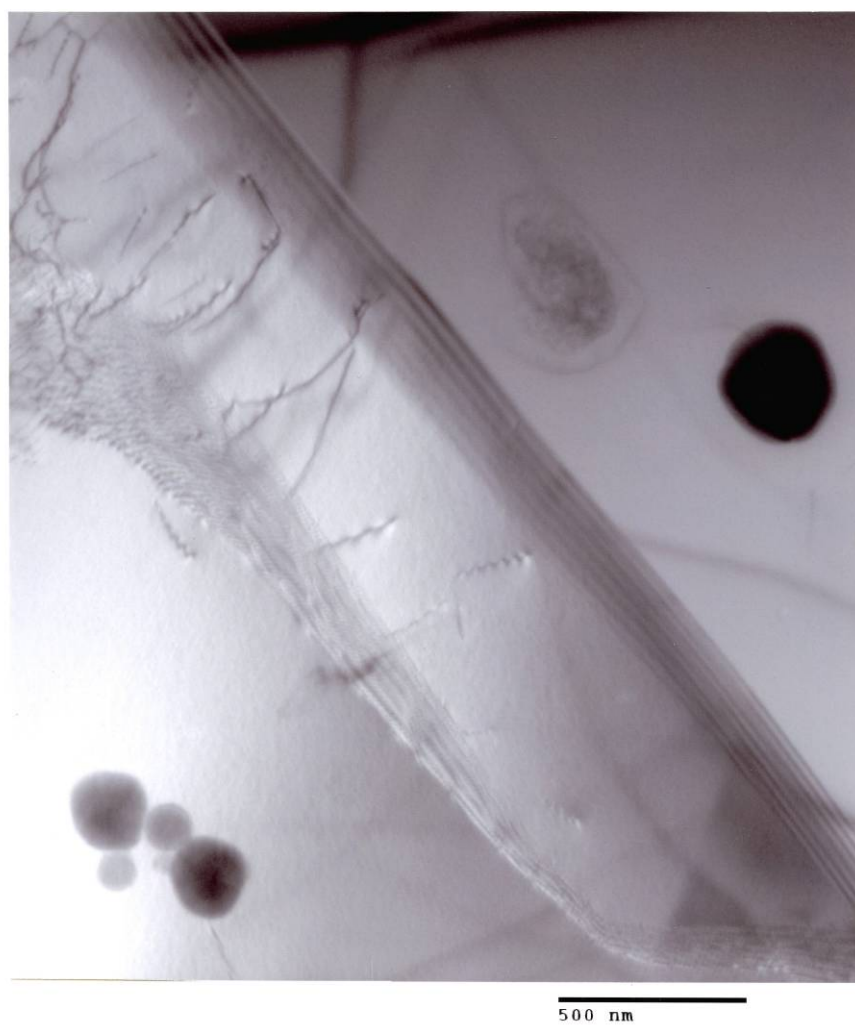
Figure 7. TEM bright-field image showing typical intragranular precipitates ($NbCr_2$) corresponding to Figure 6. Coherent annealing twin is shown in the image center (upper left to lower right)
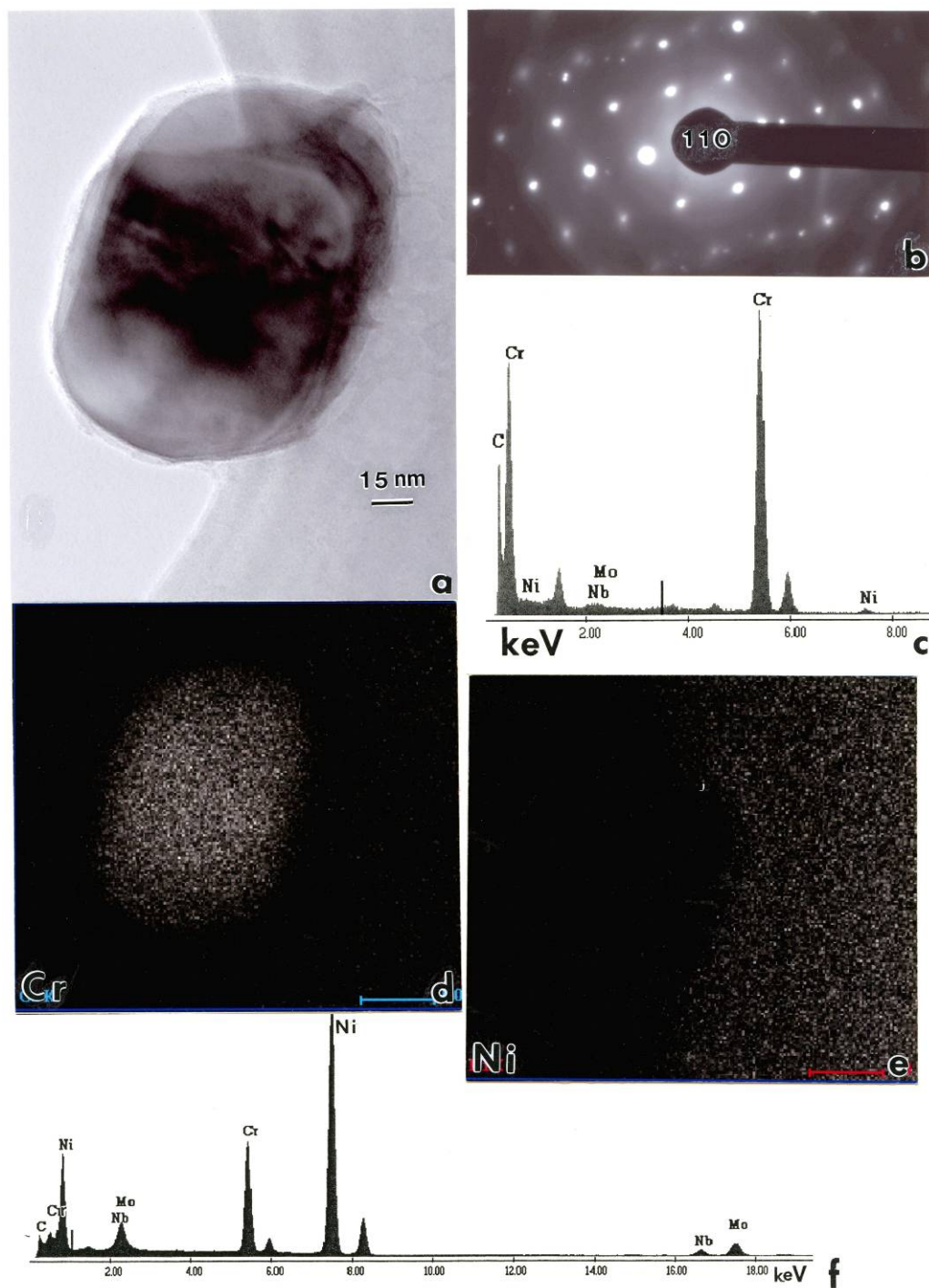
Figure 8. Analytical sequence showing Cr precipitate in EBM fabricated and HIP component. (a) TEM image of precipitate at foil edge. (b) SAED pattern showing (110) orientation for supporting NiCr matrix. (c) EDS spectra for precipitate in (a). (d) Cr map using (c). (e) Ni map for (a). (f) EDS spectrum for NiCr matrix
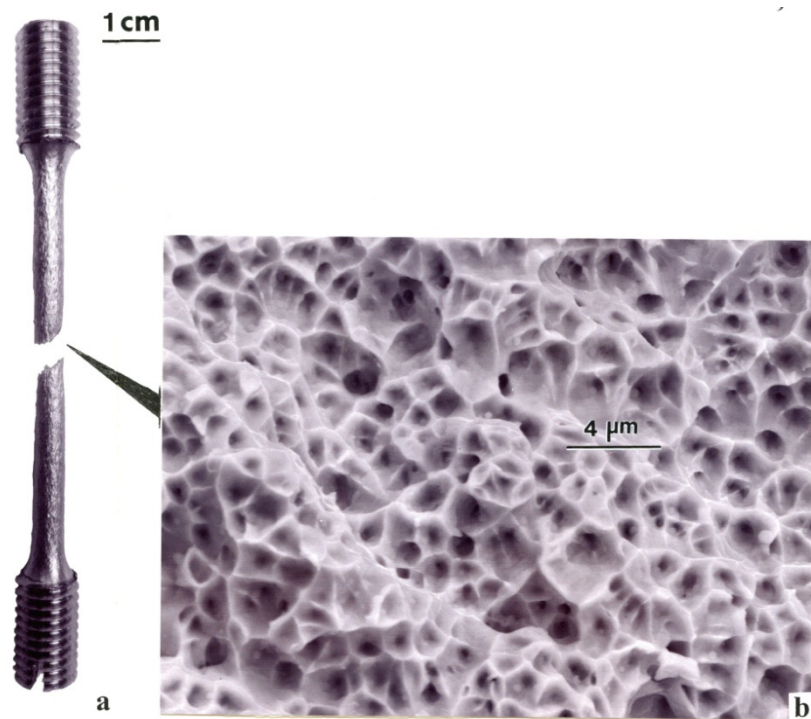
Figure 9. Failed tensile specimen for EBM fabricated and HIP component (a) and SEM image of corresponding fracture surface (b)
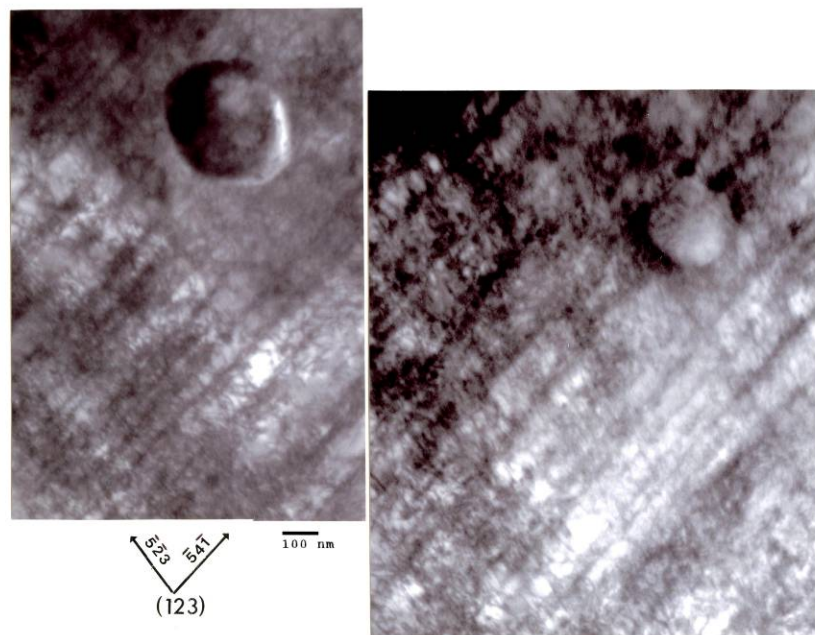
Figure 10. TEM image for failed tensile specimen in Figure 9(a) in a section ~2 mm from the fracture surface, perpendicular to the tensile axis. The two views show sections in a (123) oriented matrix grain. $NbCr_2$ precipitates are observed
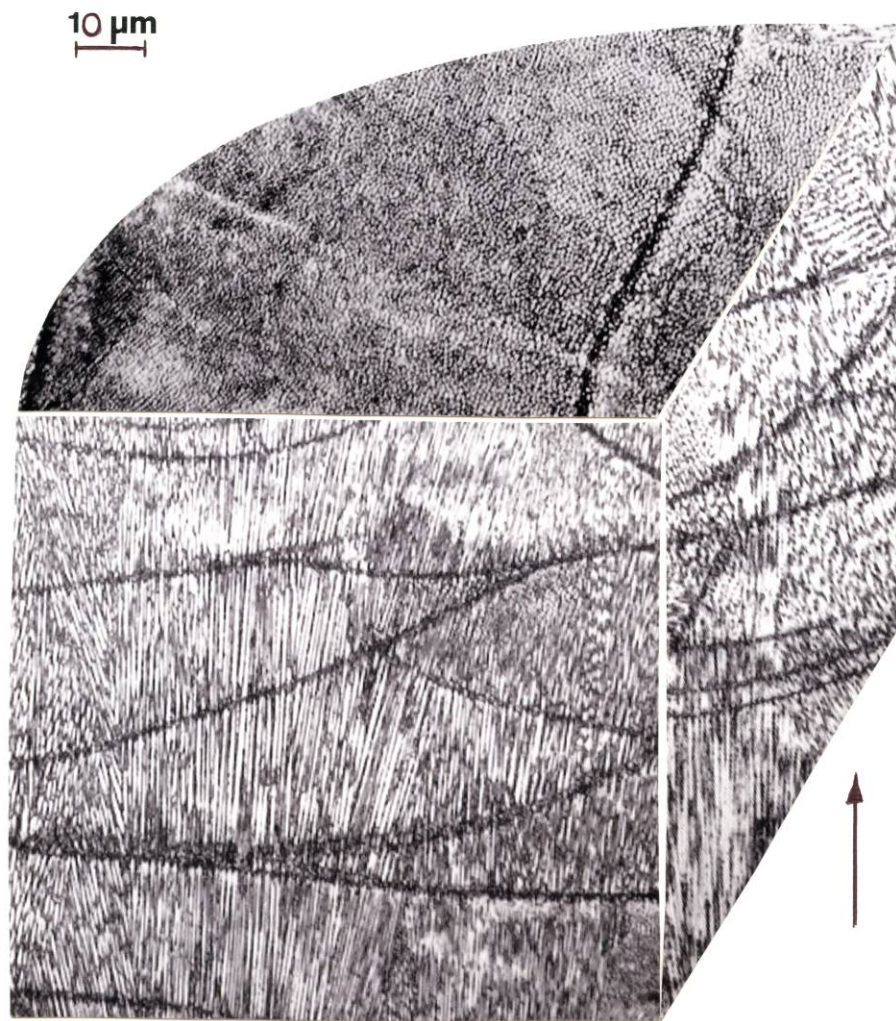
Figure 11. 3D LOM composite section for an SLM (Z-axis) fabricated component. Note build direction represented by the arrow is parallel to the Z-axis orientation
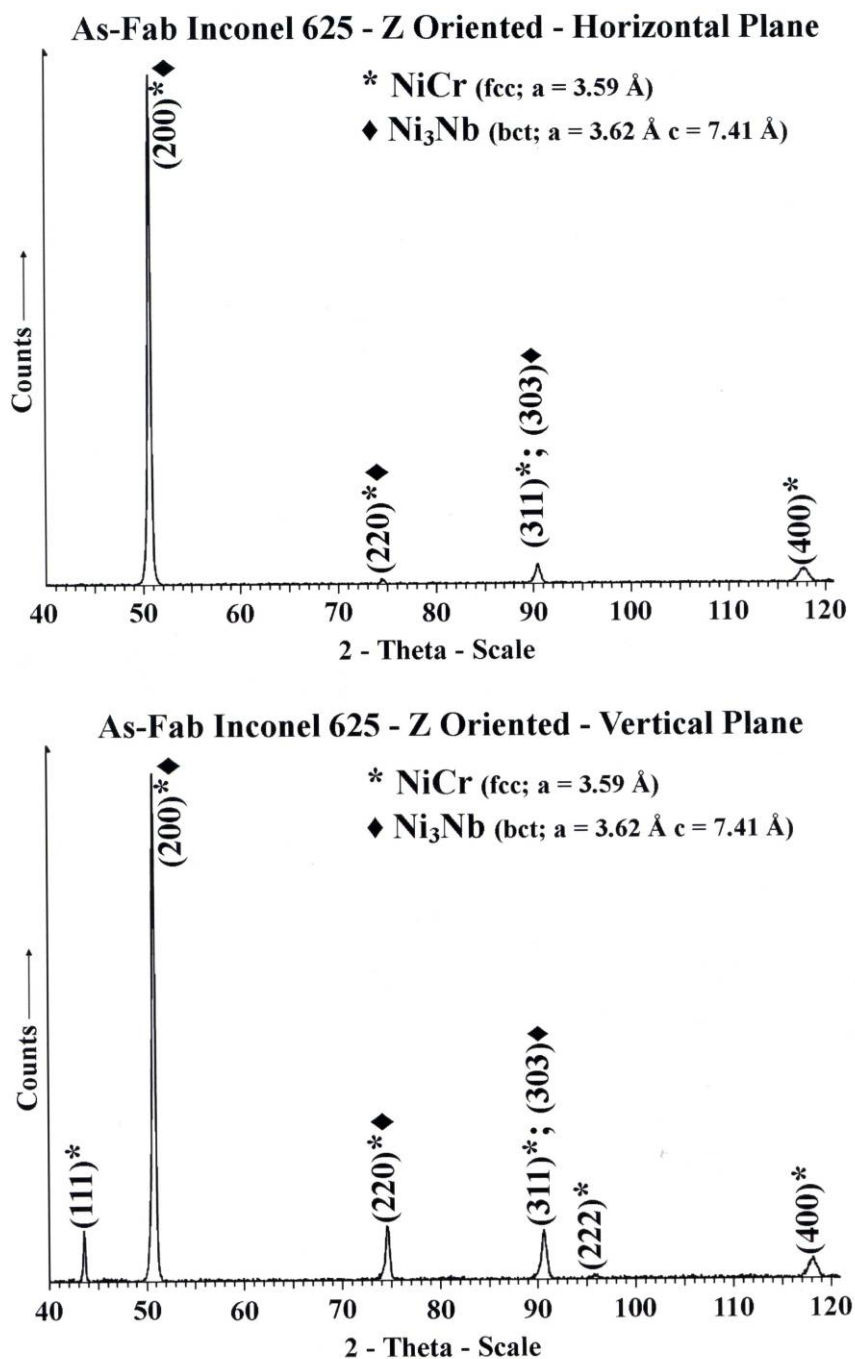
Figure 12. XRD spectrum corresponding to the vertical and horizontal reference planes represented in Figure 11
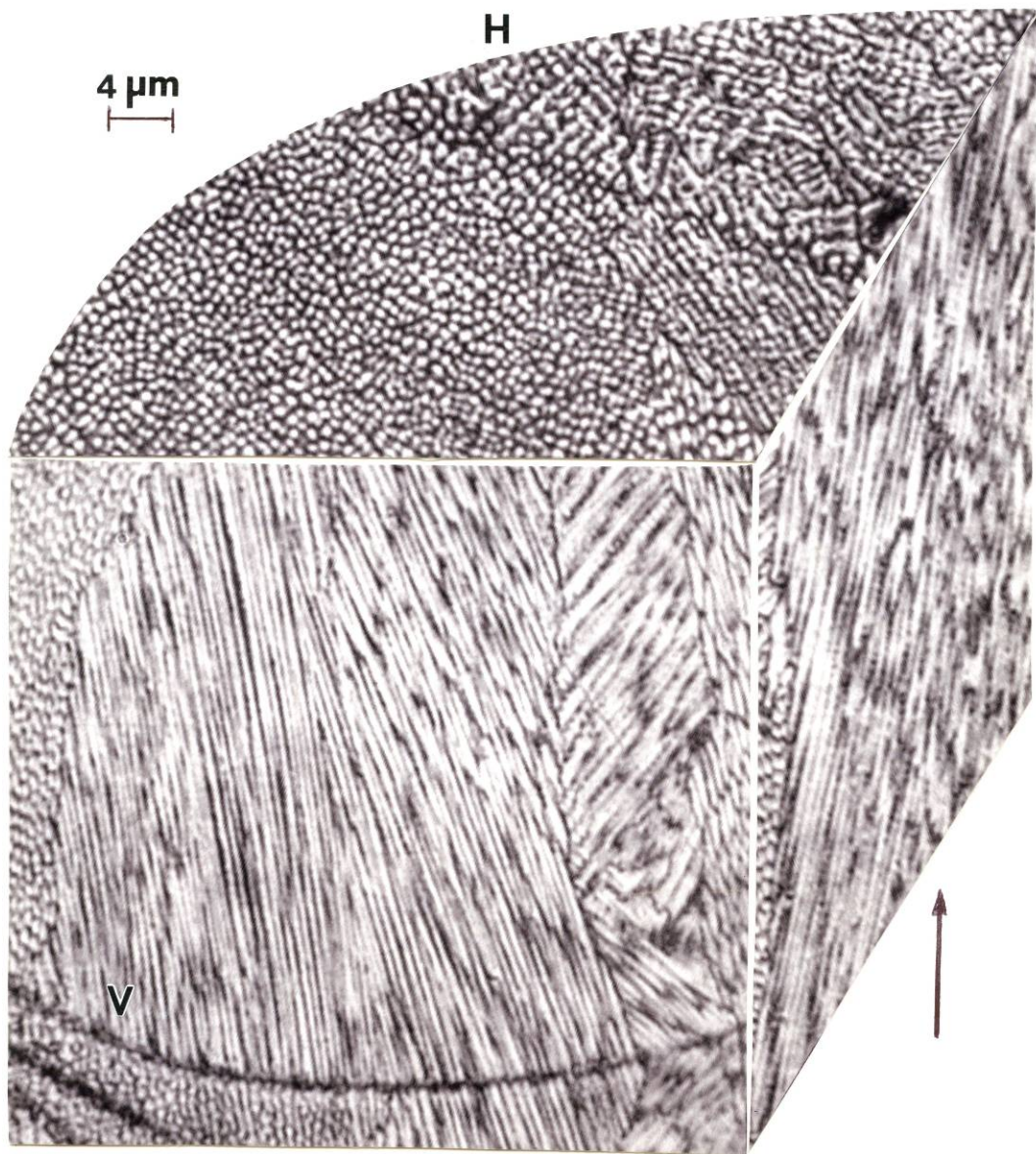
Figure 13. 3D LOM composite section for an SLM (X, Y-axis) fabricated component. Note build direction represented by the arrow at lower right which is perpendicular to the X, Y-axis, of the cylindrical component. Low-angle grain boundary is denoted GB. Melt-scan band is shown at B
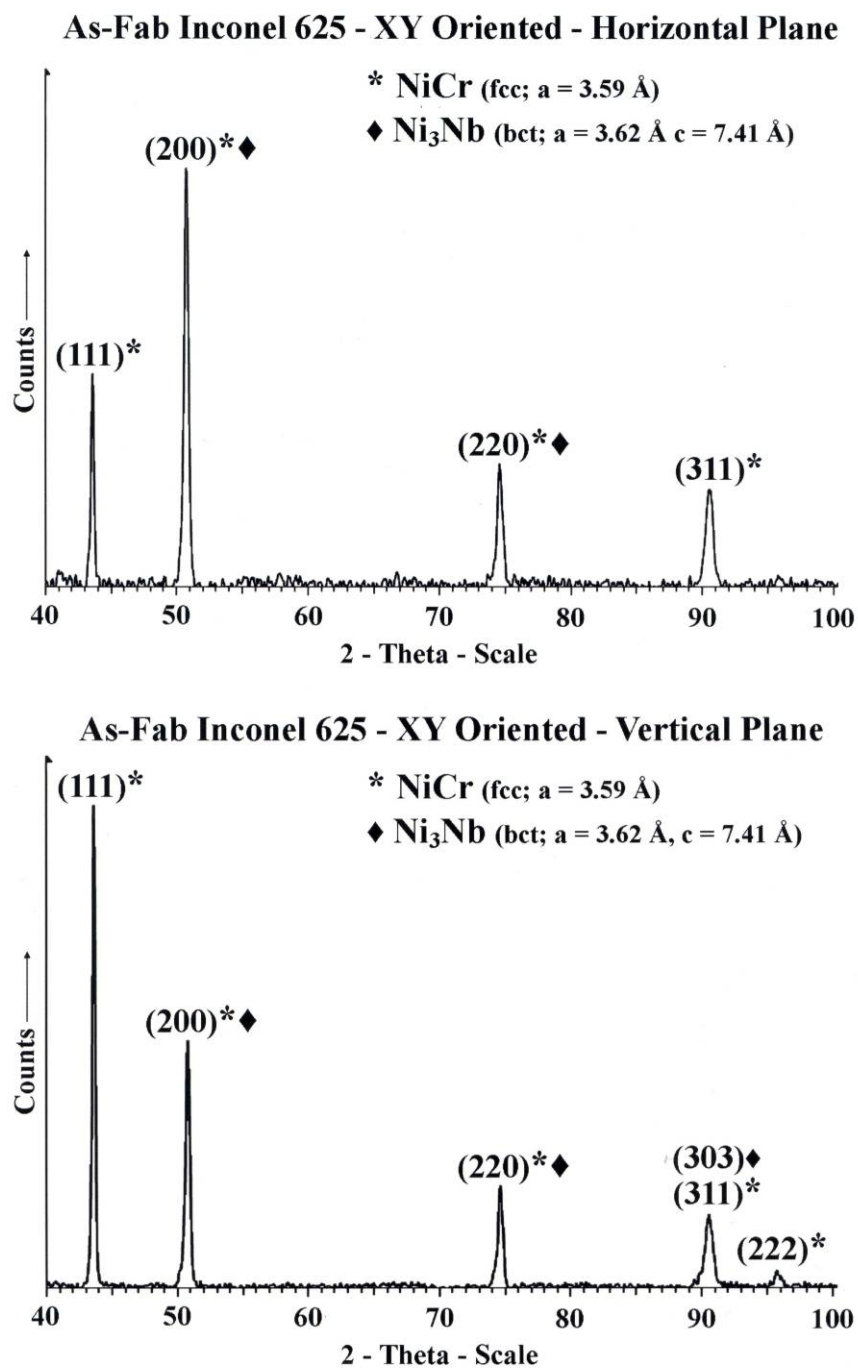
Figure 14. XRD spectrum corresponding to the vertical and horizontal reference planes represented in Figure 13
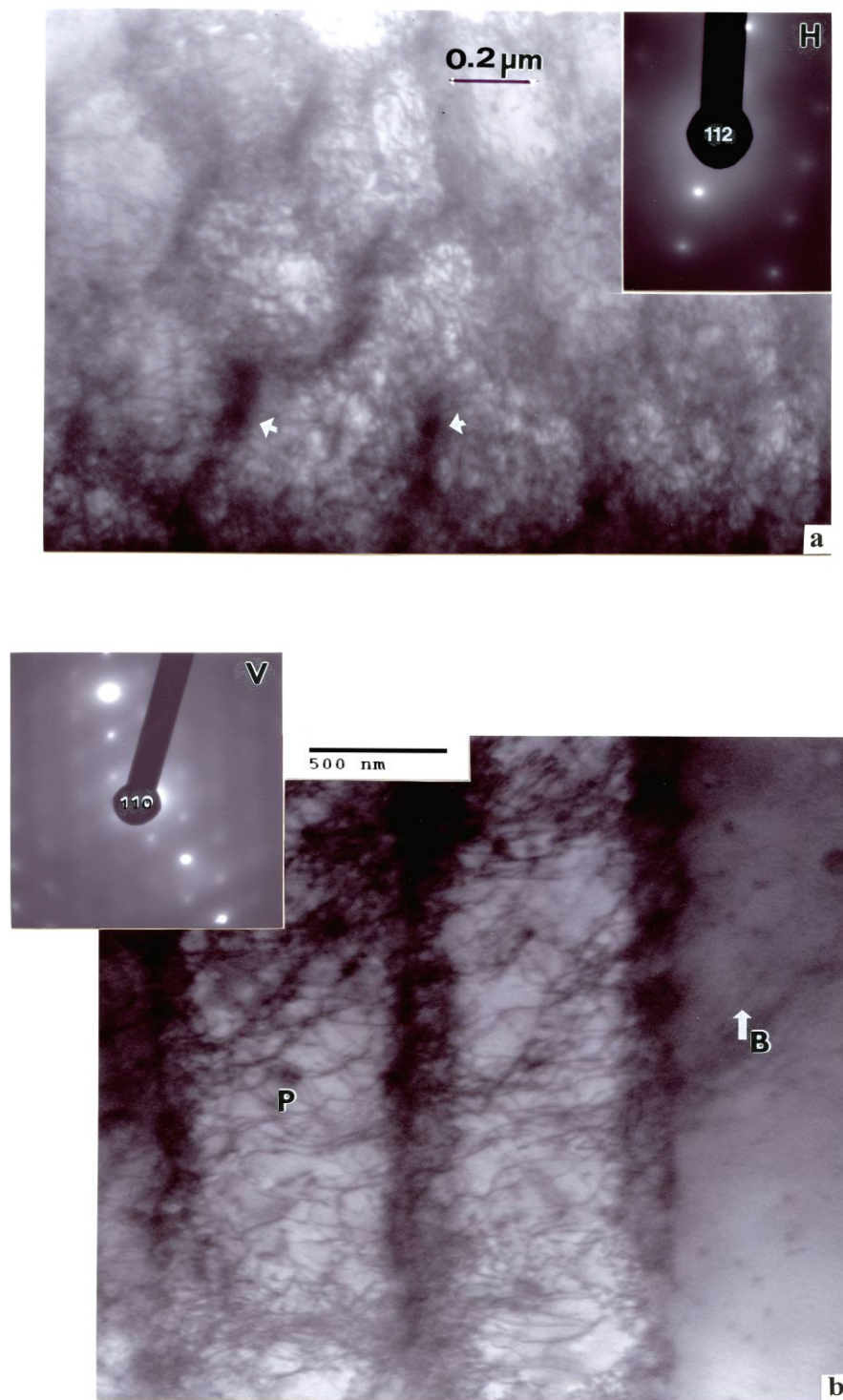
Figure 15. TEM bright-field images in the (a) horizontal (H) and (b) vertical (V) reference planes for Figure 13. P in (b) designates a precipitate (γ″) cluster. The build direction is denoted by white arrow (B) at right in (b) SAED pattern inserts show (112) orientation in the horizontal (H) plane (a), and (110) orientation in the vertical (V) plane (b). Note arrows in (a) show precipitate clusters within dislocation cell-like arrays
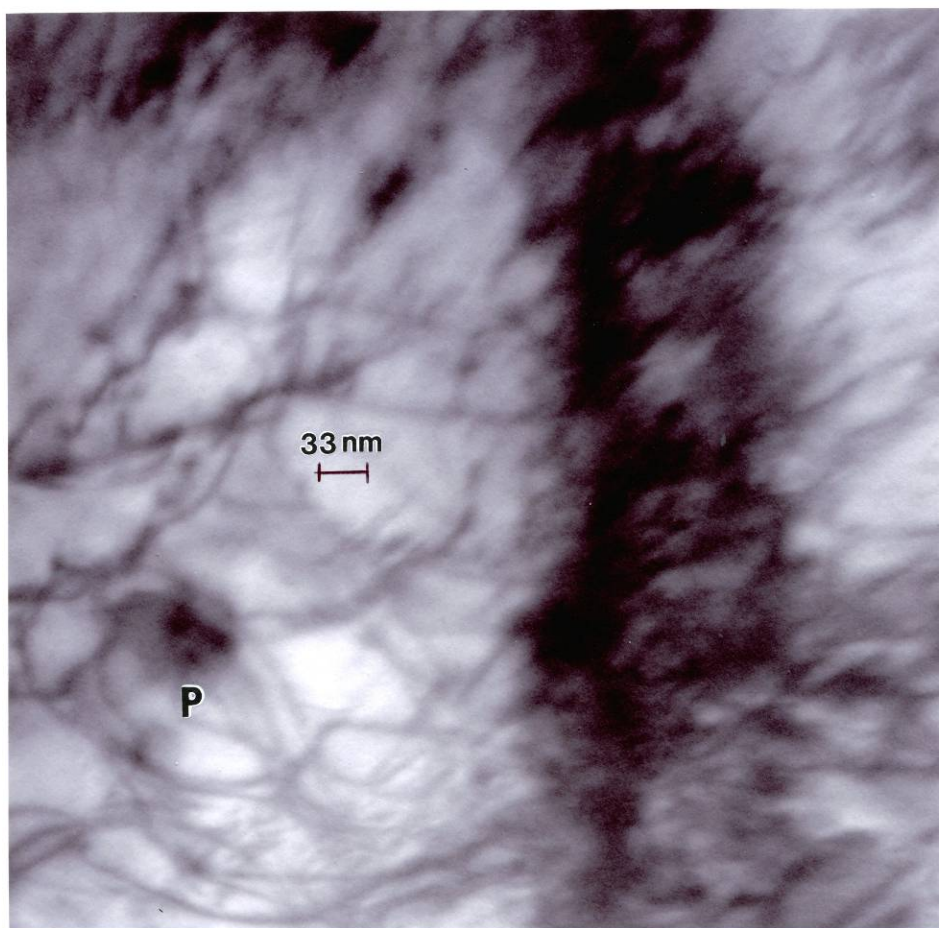
Figure 16. TEM magnified view in Figure 15, P designates precipitate cluster in Figure 15. Column of precipitate clusters and dense dislocations is shown at right
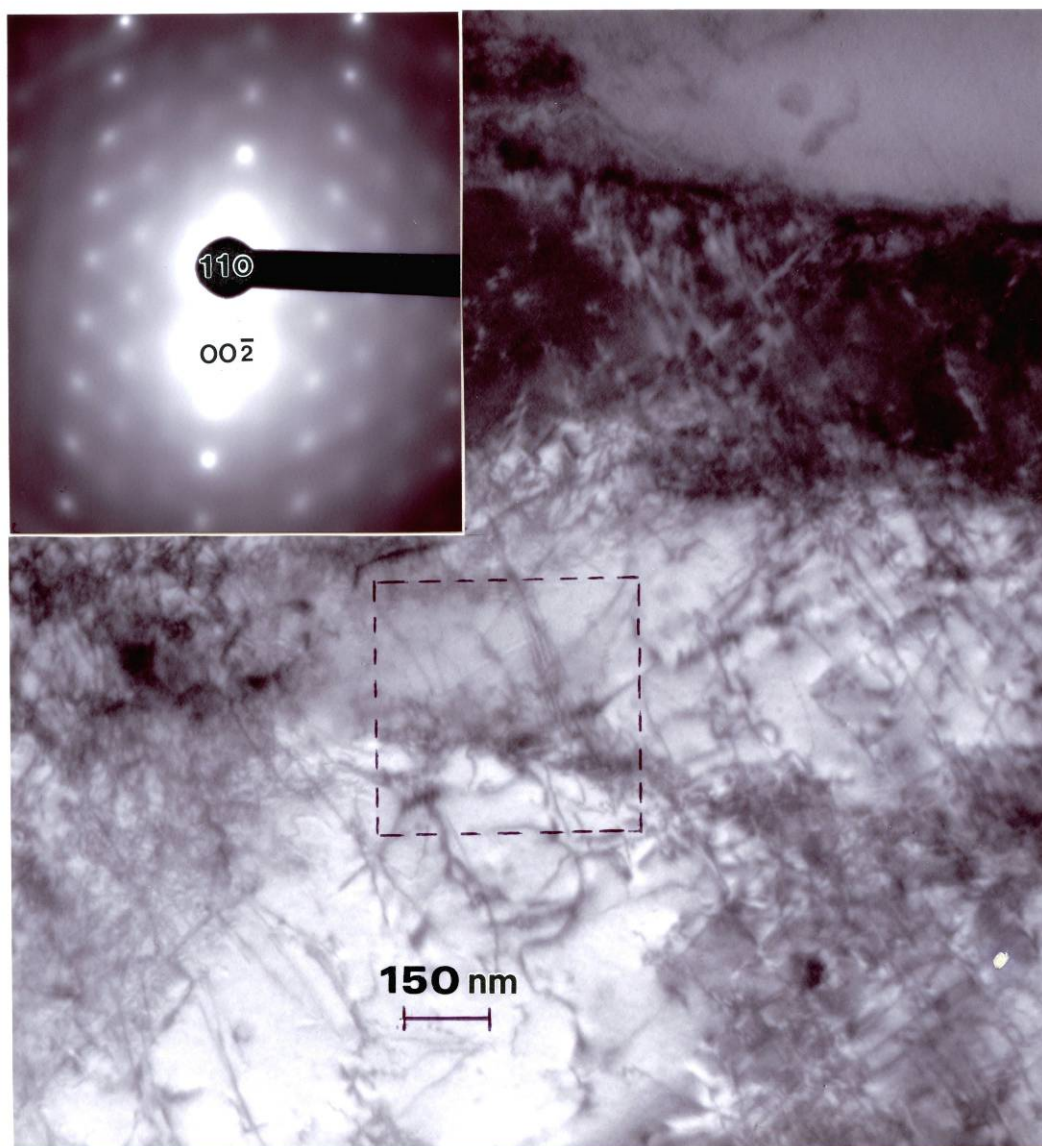
Figure 17. TEM image showing γ″ precipitation arrays. Reference section of array is enclosed in the dotted box. The SAED pattern insert shows the (110) grain surface orientation. The operating reflection for diffraction contrast is shown to be g = [00$\bar{2}$]
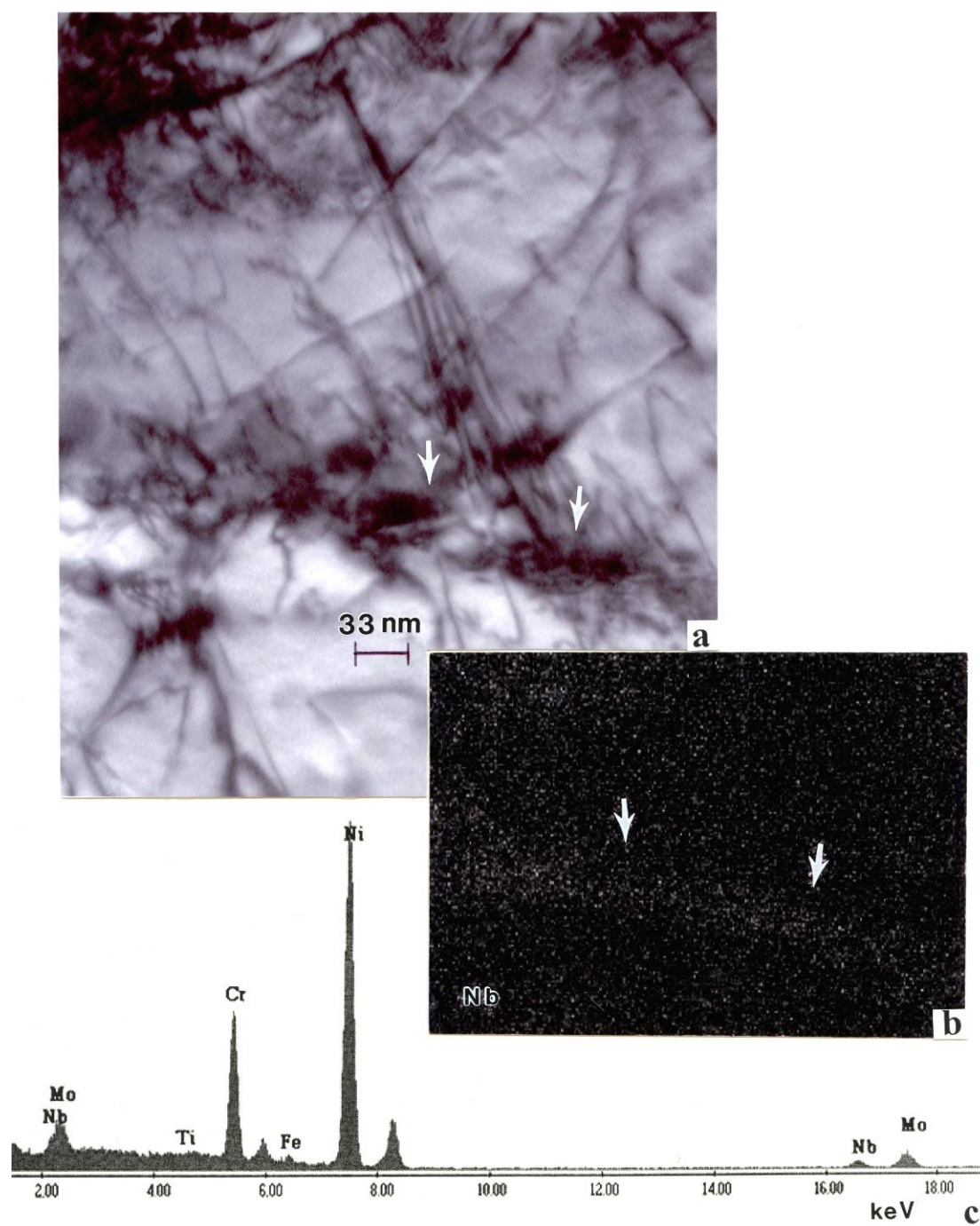
Figure 18. Magnified TEM image for Figure 17 showing precipitate clusters within the dotted reference box. Arrows in (a) show precipitate clusters (aggregates) which exhibit Nb-rich features shown in the corresponding Nb-X-ray map in (b). (c) shows the TEM-EDS spectrum for (a)
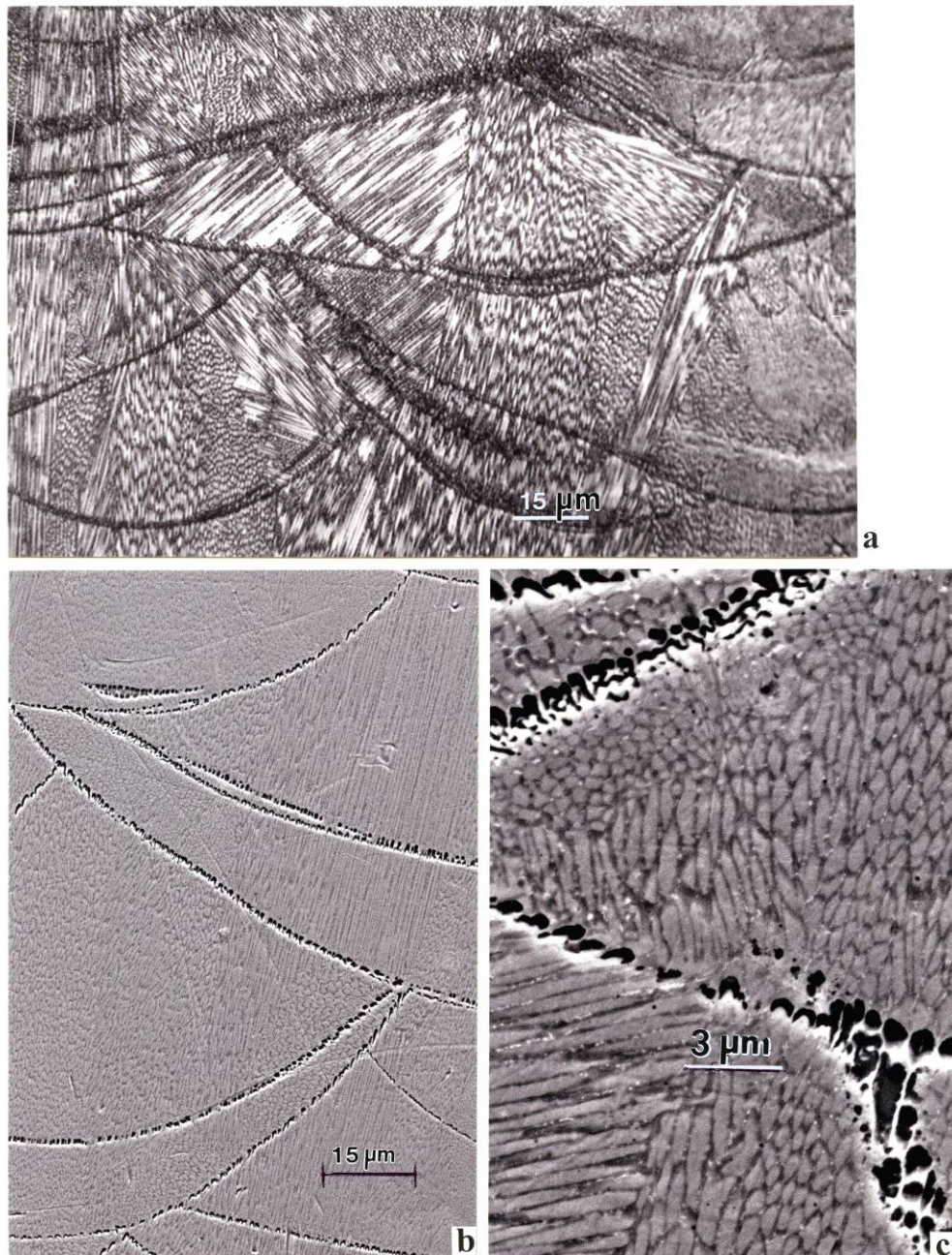
Figure 19. SLM-laser melt-scan banding. (a) LOM image in vertical reference plane for X, Y-axis cylindrical component (b) SEM image showing γ″ precipitate/second-phase formation within the melt bands. (c) Magnified SEM image showing melt-band precipitates

Figure 20. SLM fabricated and HIP (Z-axis) component 3D LOM composition showing equiaxed, fcc (NiCr) grain structure and associated precipitation
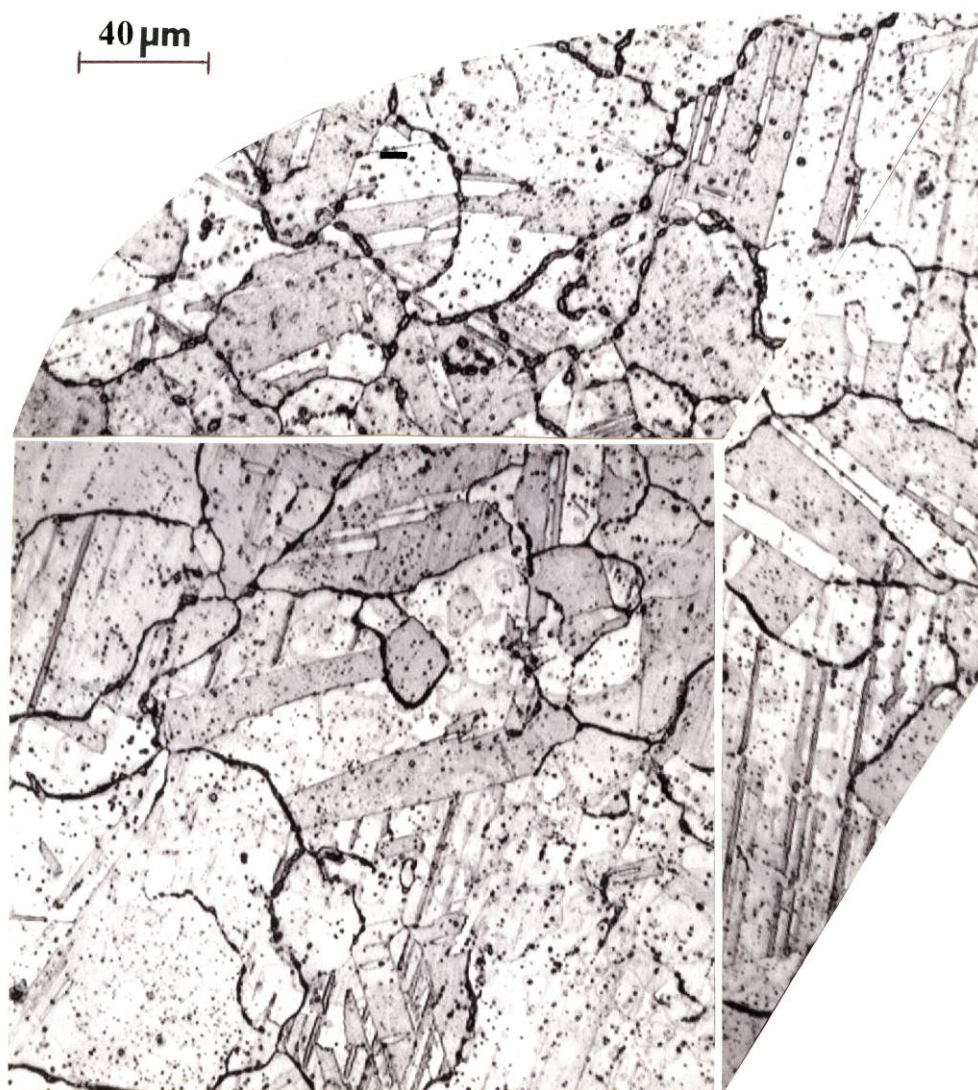
Figure 21. SLM fabricated and HIP (X, Y-axis) component 3D LOM composition showing equiaxed, fcc (NiCr) grain structure and associated precipitation
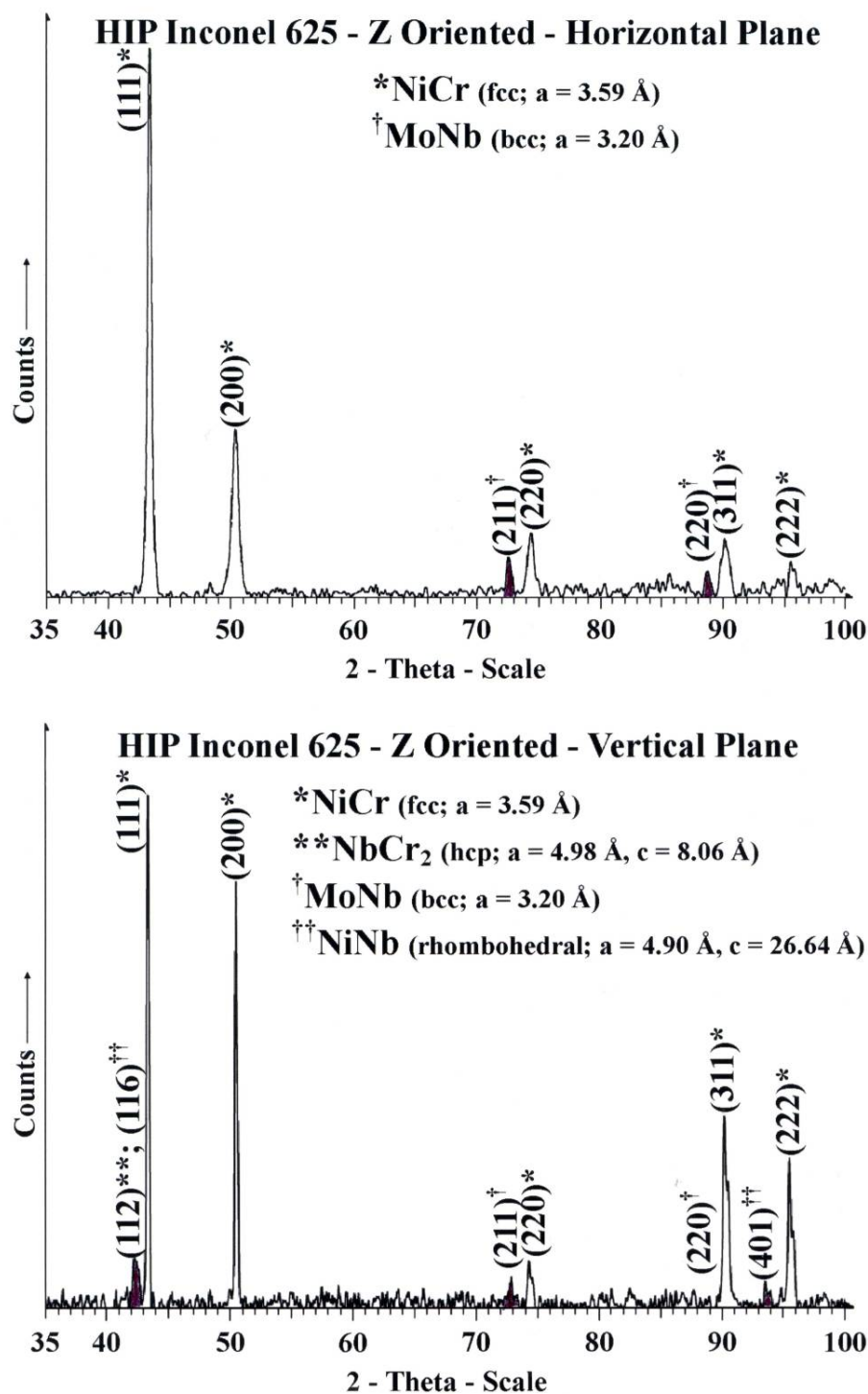
Figure 22. XRD spectra corresponding to horizontal and vertical reference planes in Figure 20. Precipitation peaks are dark shaded
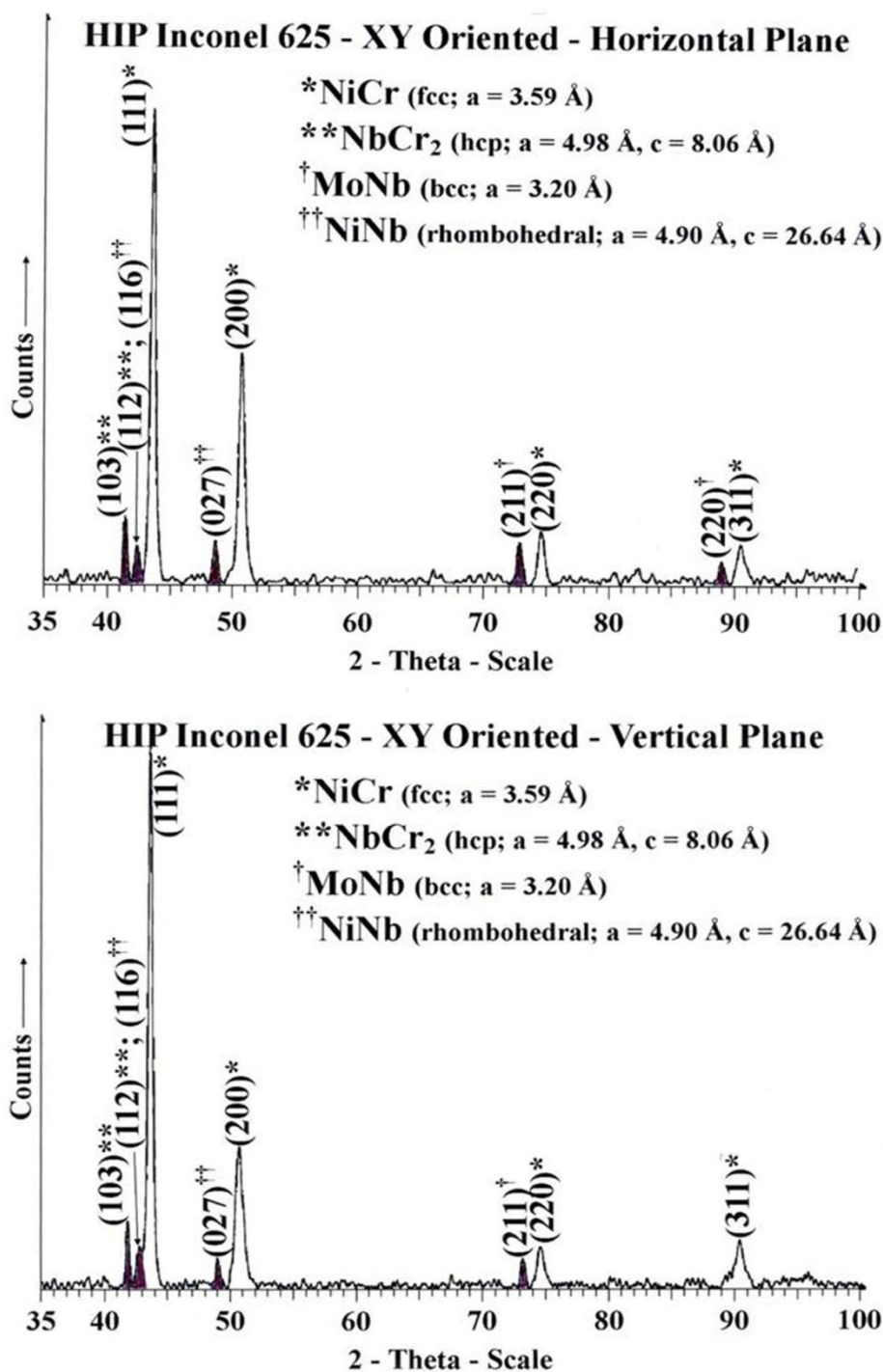
Figure 23. XRD spectra corresponding to horizontal and vertical reference planes in Figure 21. Precipitation peaks are dark shaded
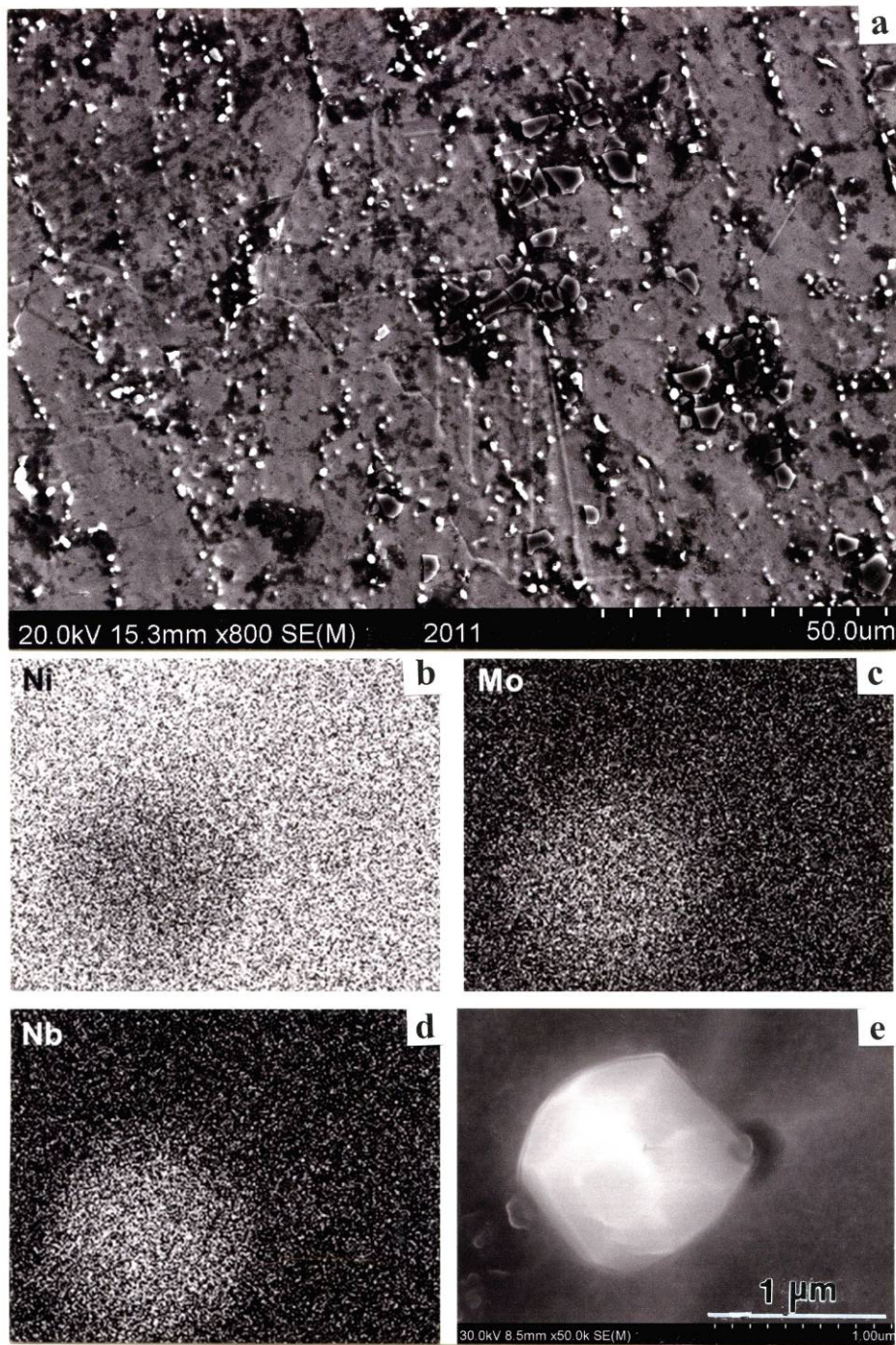
Figure 24. SLM (Z-axis) fabricated and HIP component observed in vertical reference plane (Figure 20). (a) SEM image of precipitates. (b) to (d) show corresponding EDS elemental X-ray maps. (c) Precipitate image
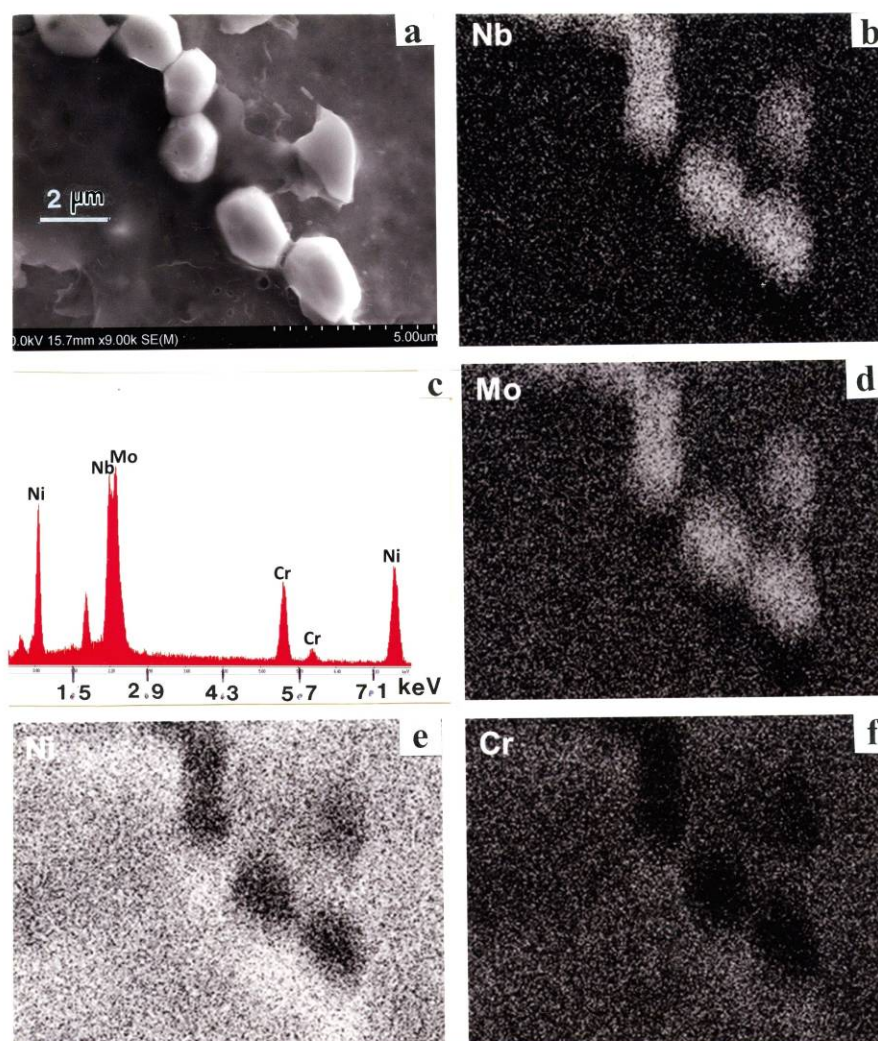
Figure 25. SEM analysis sequence corresponding to Figure 24(a). (a) Precipitates. (b) EDS spectra for (a). (c) to (f) show corresponding EDS elemental X-ray maps
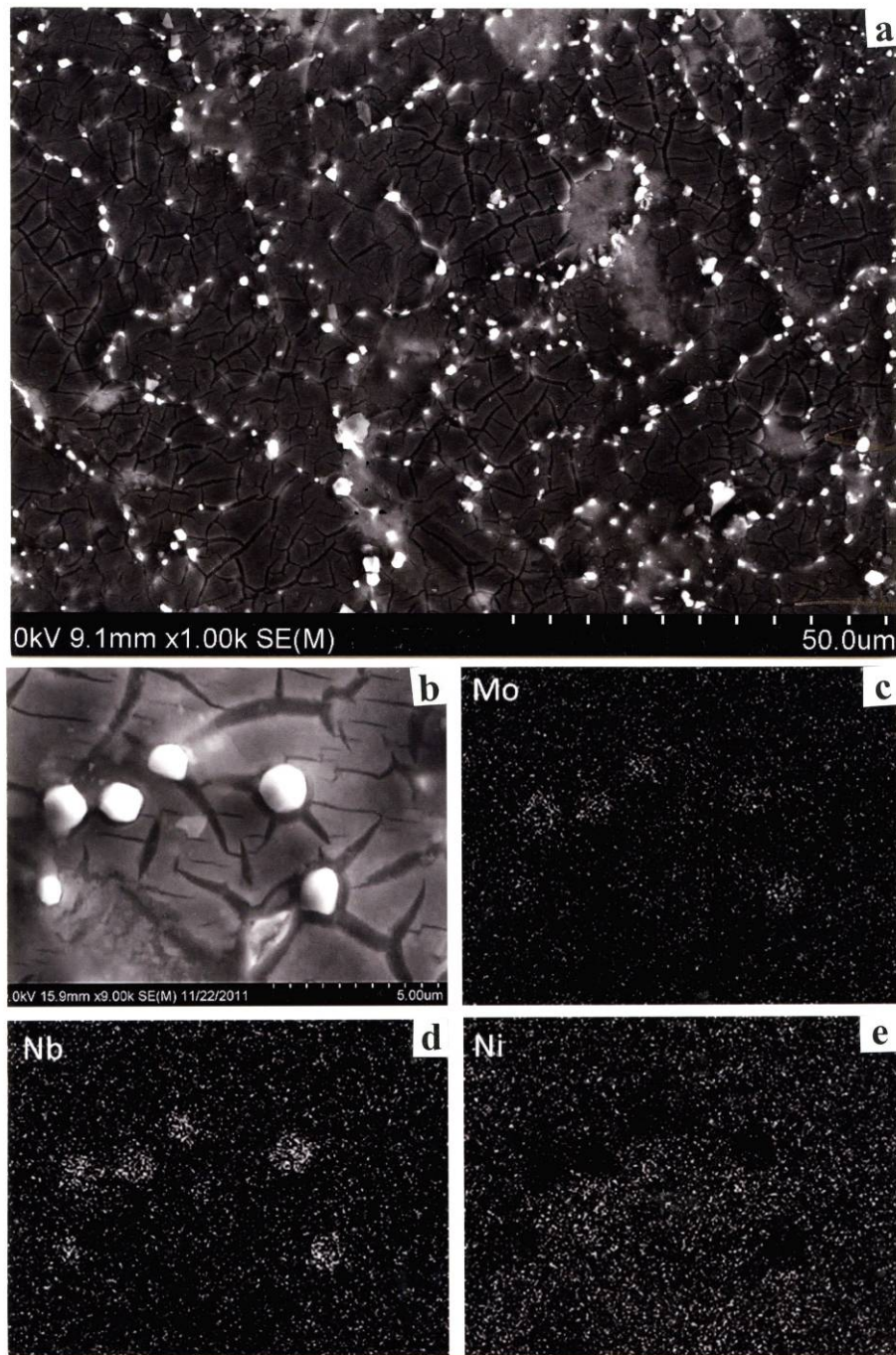
Figure 26. SEM analysis sequence corresponding to the vertical reference plane in Figure 21 (X, Y-axis) build. (a) Vertical surface view of precipitates. (b) Magnified view of precipitates. (c) to (e) show corresponding EDS elemental X-ray maps
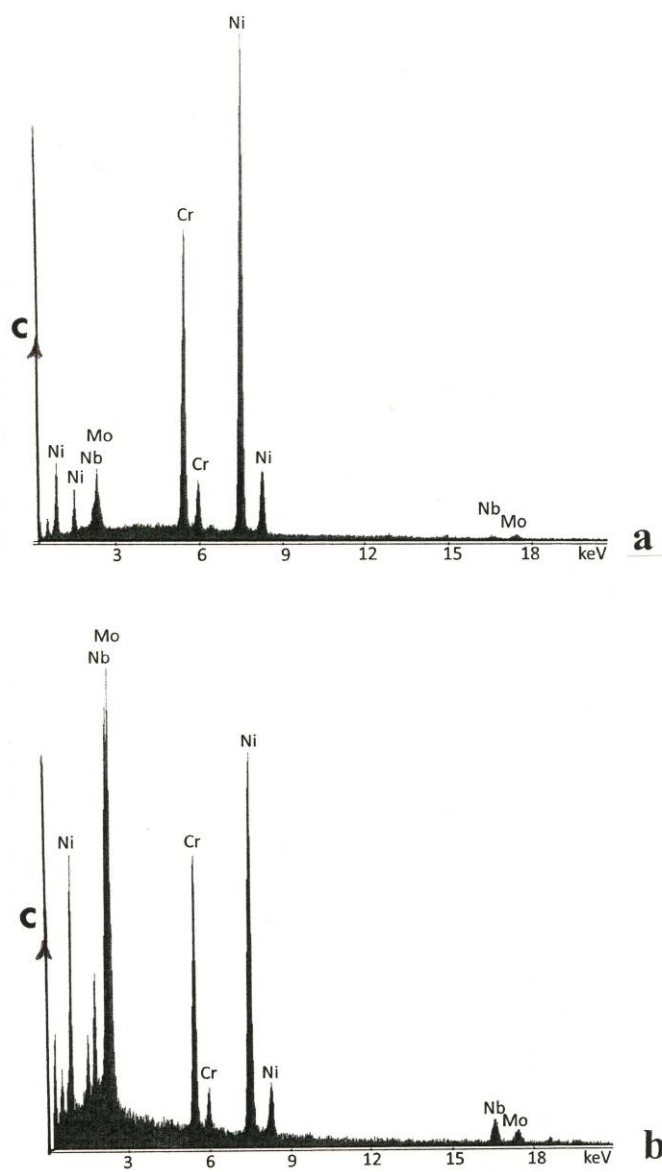
Figure 27. EDS spectra corresponding to Figure 26. (a) matrix. (b) Precipitate area as in Figure 26(b)
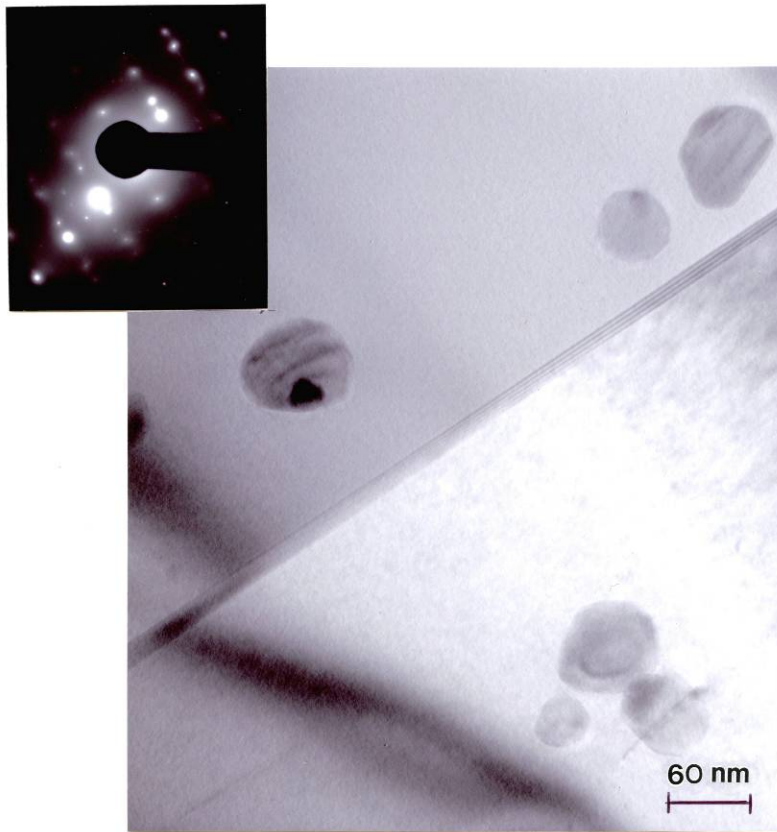
Figure 28. TEM image in horizontal reference plane corresponding to Figure 21 (X, Y-axis component). The grain surface orientation is (110) shown in SAED pattern insert. Operating reflection, g = [$\bar{1}$11]. Note diffraction spots normal to inclined twin plane in SAED pattern insert
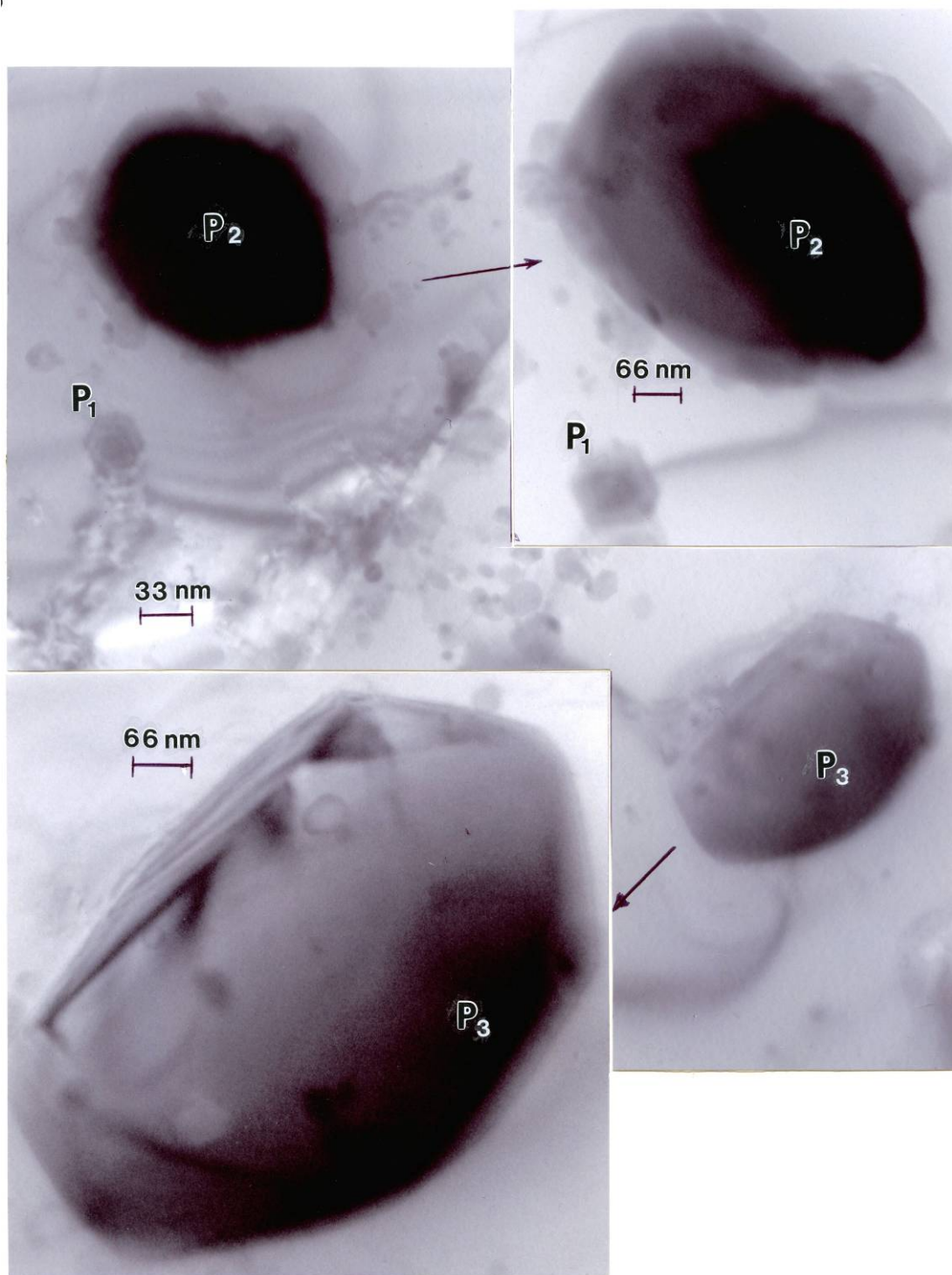
Figure 29. TEM image features for precipitates in a vertical reference plane corresponding to Figure 21. The inserts (top right and bottom left) show magnified views for precipitates marked P_1, P_2, P_3. Precipitates are single crystals dispersed nonchoherently in the fccNiCr matrix
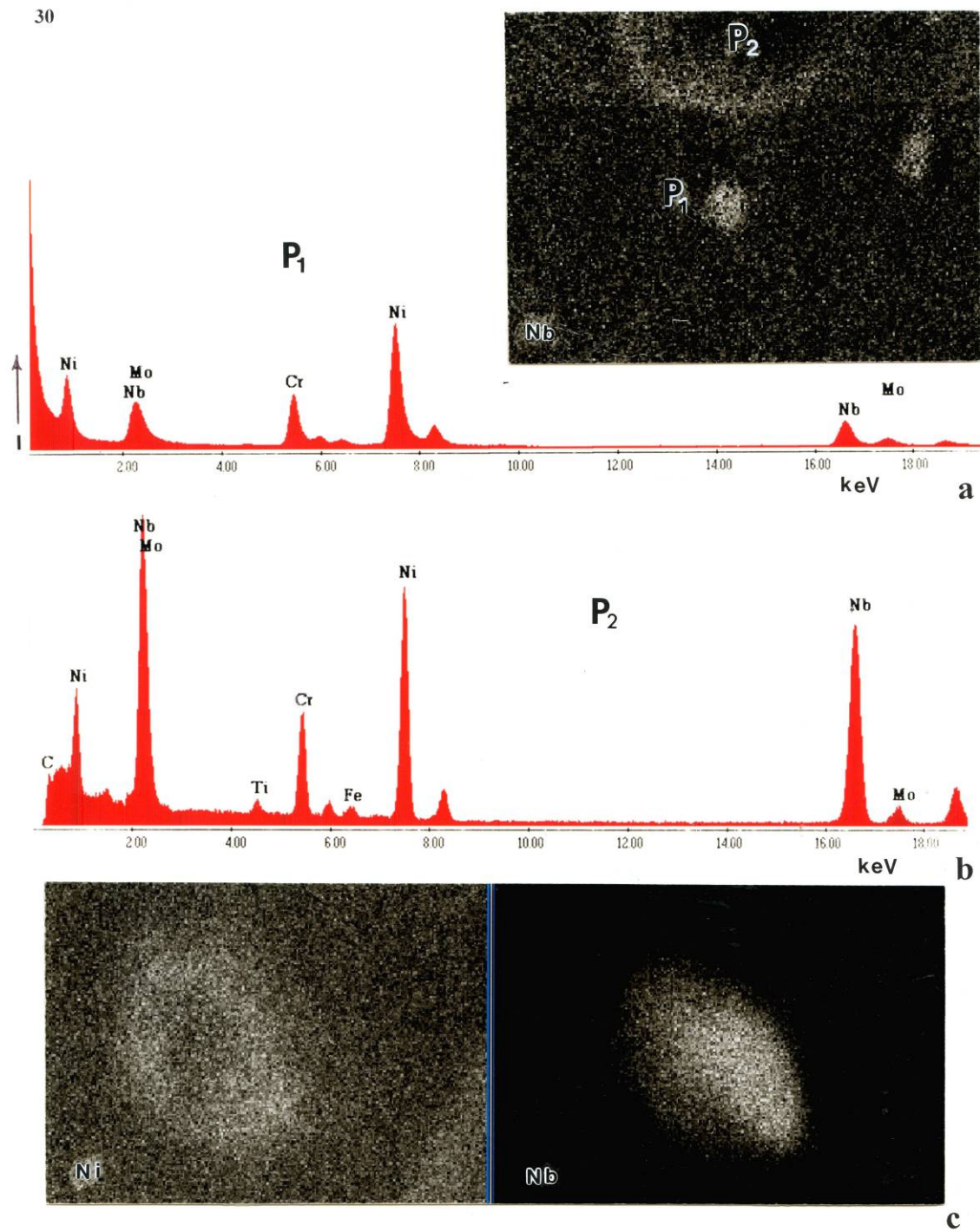
Figure 30. TEM microanalysis sequence for precipitates in Figure 29. (a) EDS analysis for precipitate P_1. Insert shows Nb characteristic X-ray map. (b) EDS analysis for precipitate P_2. (c) Ni and Nb characteristic X-ray maps for precipitate P_2 in Figure 29
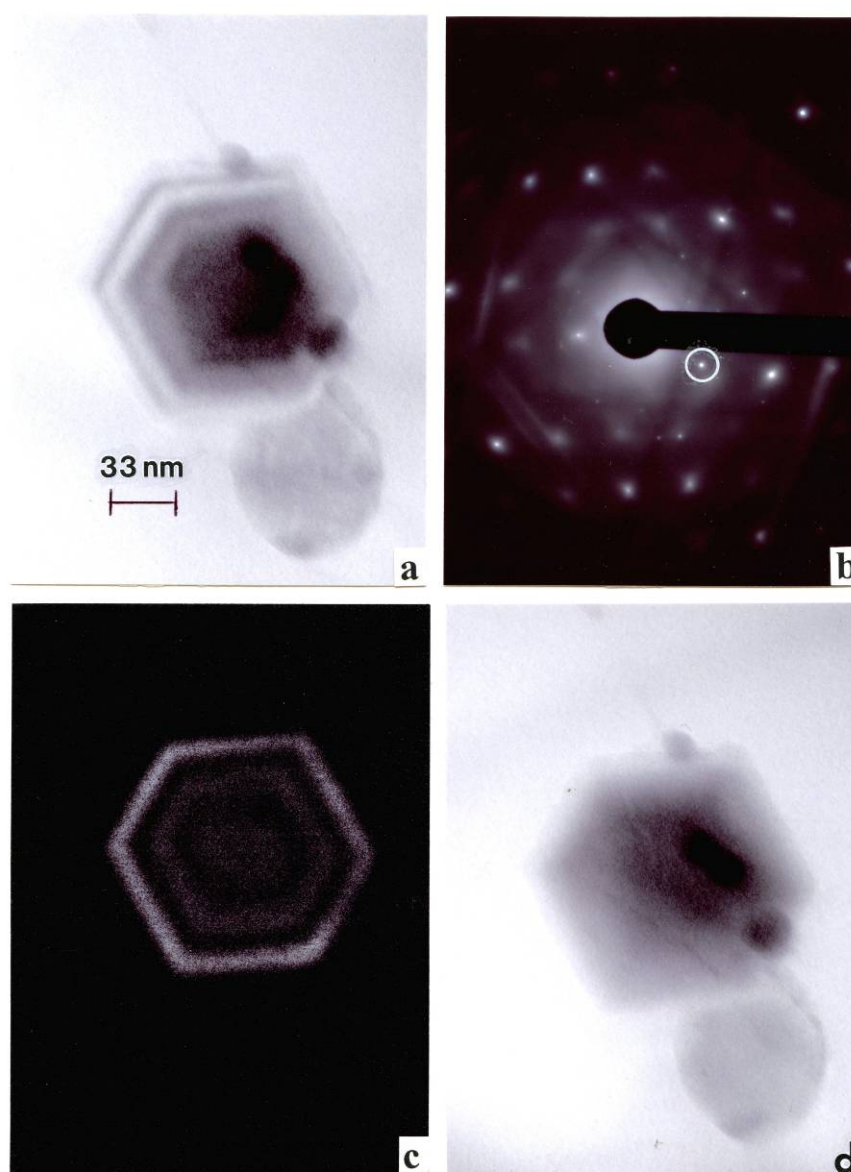
Figure 31. TEM microanalysis sequence for precipitate P_1 in Figure 29. (a) Bright-field image. (b) SAED pattern for (a). (c) Dark-field image of (a) using $[\bar{2}\bar{4}6]$ diffraction spot circled in (b). (d) Tilted bright-field image of (a)